Spatiotemporal heterogeneity in the increase of ocean acidity extremes in the Northeast Pacific

Flora Desmet[1], Matthias Münnich[1], and Nicolas Gruber[1]

[1]Environmental Physics, Institute of Biogeochemistry and Pollutant Dynamics, ETH Zurich, Universitätstrasse 16, 8092 Zürich, Switzerland

Correspondence: Flora Desmet (flora.desmet@usys.ethz.ch)

Abstract.

The acidification of the ocean (OA) increases the frequency and intensity of ocean acidity extreme events (OAXs), but this increase is not occurring homogeneously in time and space. Here we use daily output from a hindcast simulation with a high-resolution regional ocean model coupled to a biogeochemical-ecosystem model (ROMS-BEC) to investigate this heterogeneity in the progression of OAX in the upper 250 m of the Northeast Pacific from 1984 to 2019. OAX are defined using a relative threshold approach and using a fixed baseline. Concretely, conditions are considered extreme when the hydrogen ion concentration ($[H^+]$) exceeds the 99th percentile of its distribution in the baseline simulation where atmospheric CO_2 was held at its 1979 level. Within the 36 years of our hindcast simulation, the increase in atmospheric CO_2 causes a strong increase in OAX volume, duration, and intensity throughout the upper 250 m. The increases are most accentuated near the surface, with 88 % of the surface area experiencing near permanent extreme conditions in 2019. At the same time, a larger fraction of the OAX become undersaturated with respect to aragonite ($\Omega_A < 1$), with some regions experiencing increases up to nearly 50 % in their subsurface. There is substantial regional heterogeneity in the progression of OAX, with the fraction of OAX volume across the top 250 m increasing in the Central Northeast Pacific up to 160-times, while the deeper layers of the nearshore regions experience "only" a 4-fold increase. Throughout the upper 50 m of the Northeast Pacific, OAXs increase relatively linearly with time, but sudden rapid increases in yearly extreme days are simulated to occur in the thermocline of the far offshore regions of the Central Northeast Pacific. These differences largely emerge from the spatial heterogeneity in the local $[H^+]$ variability. The limited offshore reach of offshore propagating mesoscale eddies, that are an important driver of subsurface OAX in the Northeast Pacific, causes a sharp transition in the increase of OAX between the rather variable thermocline waters of nearshore regions and the very invariant waters of the Central Northeast Pacific. The spatially and temporal heterogeneous increases in OAX, including the abrupt appearance of near permanent extremes, likely have negative effects on the ability of marine organisms to adapt to the progression of OA and its associated extremes.

1 Introduction

Ocean uptake of anthropogenic carbon dioxide (CO_2) from the atmosphere is the main driver of the ongoing surface ocean acidification (OA), that is the long-term increase in the hydrogen ion concentration $[H^+]$ and the decreases in pH (with pH=-

log($[H^+]$)) and aragonite saturation state (Ω_A) in the surface ocean (Hoegh-Guldberg et al., 2018; Bindoff et al., 2019; Doney et al., 2009; Caldeira and Wickett, 2003). These trends are bound to increase the occurrence of ocean acidity extreme events (OAXs). But how such extremes progress and what this means in terms of their average duration, frequency, and intensity, has only been analyzed by a handful of model-based studies so far (Gruber et al., 2021; Burger et al., 2020; Hauri et al., 2013a; Negrete-García et al., 2019), primarily due to the lack of long and high spatiotemporal resolution observational records of ocean carbonate chemistry variables.

OAXs are defined as either rare and unusually high (low) $[H^+]$ (pH, Ω_A) events (Desmet et al., 2022; Gruber et al., 2021; Burger et al., 2020, 2022) or events when the $[H^+]$ concentration (pH, Ω_A) is above (below) a given absolute threshold known to be harmful to certain marine organisms (Hauri et al., 2013a). The rareness of events is usually determined by requiring events to cross a "extreme" relative threshold, often determined from a certain percentile (e.g., 1st or 99th) of a cumulative frequency distribution (Seneviratne et al., 2012; Gruber et al., 2021). The frequency distribution itself is obtained by sampling the environmental conditions over a certain baseline period (Oliver et al., 2021). Irrespective of the choice of absolute or relative thresholds to identify extremes, all studies conducted so far have confirmed that OAXs have become already more frequent, longer, and more intense since the preindustrial era and that these trends will continue in the future (Burger et al., 2020; Gruber et al., 2021; Hauri et al., 2013a). They have also confirmed that the main driver of these changes is the increase in atmospheric CO_2 driving an increase in the surface ocean concentration of anthropogenic CO_2. For example, between the preindustrial period and the recent decades, the number of surface extreme days for $[H^+]$ across the global surface ocean was shown to increase from ~4 to ~300 days a year for OAX defined using a relative threshold on a fixed preindustrial baseline (Burger et al., 2020). A similar increase was simulated at 200 m depth. While this global-scale increase is very large, it was found to occur relatively smoothly in time (Burger et al., 2020; Gruber et al., 2021). Yet, this might not be the case at the regional scale, where variability is larger. But so far, limited emphasis has been given to such potential spatial and temporal heterogeneities in the progression of OAX, and the potential for abrupt changes. This is in part a consequence of the fact that the global studies used relatively coarse-resolution Earth system models, which do not resolve mesoscale variability that has been shown to be rather relevant for generating OAX (Desmet et al., 2022).

In fact, such abrupt changes in OAX have been detected at the regional scale in the California and Humboldt Current Systems (Hauri et al., 2013a; Franco et al., 2018) and in the Southern Ocean (Hauri et al., 2015; Negrete-García et al., 2019). These OAXs, defined in these studies as undersaturation events where $\Omega_A < 1$, exhibit abrupt onsets, non-linear increases, and sudden shoalings. For example, in the nearshore bottom waters off California, Hauri et al. (2013a) showed that while the median duration of such undersaturation events increased only modestly up to the year 2000, these events abruptly become near permanent in the ensuing decades. Such abrupt increase may also occur for OAX defined using relative thresholds, i.e., when the environmental conditions suddenly shift to conditions outside the previously established variability ranges. Such an abrupt increase in OAX could have especially deleterious effects on marine organisms since they are not only exposed to conditions that are outside the variability that they are adapted to (Vargas et al., 2017, 2022; Kroeker et al., 2020; Rivest et al., 2017;

Cornwall et al., 2020), but are also forced to transition to the new conditions at a speed that likely exceeds their capacity to adapt (Gruber et al., 2021).

The rate and potential abruptness of the increase in OAX in response to the rise in atmospheric CO_2 is likely to vary between regions and depths owing to differences in the rate of change of the underlying variables of the marine carbonate system (Ma et al., 2023) and because of differences in the magnitude and type of variability of these variables (Sutton et al., 2019; Carter et al., 2019; Keller et al., 2014). Owing the generally Gaussian-type distribution of environmental conditions, the same shifts in the underlying distribution impact extremes very differently in high versus low variability regions. We generally expect that regions characterized by large variability tend to experience smaller increases in OAX than regions with low variability. The same underlying concept is captured by the time of emergence (ToE) concept, which is the time for the trend in OA to exceed the background variability (Sutton et al., 2019; Turk et al., 2019; Carter et al., 2019; Keller et al., 2014). This means that after the ToE has passed, the change is clearly detectable and the conditions are, on average, very different from anything in the past. Thus, the ToE in open ocean sites that are characterized by low variability tend to be much shorter than those in coastal sites, where variability is high (Sutton et al., 2019; Turk et al., 2019; Carter et al., 2019; Keller et al., 2014). This also means that we expect the largest changes in OAX in the open ocean regions characterized by low variability. For abruptness, the relationship with variability is not so clear, since this metric strongly depends on the details of the variability and of the nature of the underlying change of the marine carbonate system variable of interest. Still, low variability regions might be more prone to abrupt changes than those characterized by high variability.

Of particular relevance with respect to OAX is the eastern North Pacific, due to its vulnerability to OA. Waters naturally low in pH and Ω_A make up the upper 250 m depth, particularly inshore along the Alaskan, Canadian, and U.S. West Coasts where the saturation horizon with regard to aragonite is naturally shallow (Jiang et al., 2015; Byrne et al., 2010; Feely and Chen, 1982; Feely et al., 2008). Besides, observation and model-based studies found rapid acidification in those regions (Jiang et al., 2019; Gruber et al., 2012; Hauri et al., 2013b; Turi et al., 2016), threatening important marine ecosystems and their services since the region hosts highly productive waters and important fisheries, including OA sensitive species (Mundy, 2005; Messié et al., 2009; Pauly and Christensen, 1995; Bednaršek et al., 2014, 2017, 2020; Long et al., 2016; Swiney et al., 2016; Williams et al., 2019).

Spatial patterns and regional drivers of OAX in the Northeast Pacific have been investigated recently in a regional ocean model that explicitly resolves mesoscale variability (Desmet et al., 2022). Within the upper 100 m, westward propagating mesoscale cyclonic eddies were found to drive the largest and longest tracked OAX, defined as combined unusually low pH-Ω_A space-time events, revealing the key role of mesoscale variability in OAX formation and sustenance. Hence, in the California current system (CCS) as well as hundreds of kilometers offshore, OAXs are shaped by the extensive mesoscale activity of the CCS (Desmet et al., 2022; Zhao et al., 2021; Chabert et al., 2021; Combes et al., 2013; Nagai et al., 2015; Amos et al., 2019; Chenillat et al., 2016). Near the U.S. West Coast, shallow and intense OAXs emerge from seasonal upwelling,

95   which confers high pH and Ω_A natural variability to the waters (Desmet et al., 2022; Fassbender et al., 2011, 2018; Turi et al.,
2014). Therefore, leading drivers of OAX in the Northeast Pacific differ across space, with different scales of variability pre-
dominating, likely to drive a spatially heterogeneous temporal progression of OAX in response to the rise in atmospheric CO_2.

In the present study, we quantify the rate, the abruptness, and the heterogeneity of the increase in OAX across the upper
100 ocean of the Northeast Pacific. We thereby use a high-resolution mesoscale-resolving oceanic model, focus on the period from
1984 through 2019, and adopt a relative threshold definition of the OAX on the basis of the [H^+] concentration. We also
attribute which fraction of the change is due to the rise in atmospheric CO_2.

2 Methods

2.1 Simulations

105 This study is based on the UCLA-ETH version of the Regional Oceanic Modeling System (ROMS) (Shchepetkin and McWilliams,
2005) coupled to the biogeochemical ecosystem model BEC (Frischknecht et al., 2018; Moore et al., 2013). We use the same
model configuration and forcing as described by Desmet et al. (2022) and we refer the reader to that study for further details.
An important feature of our model configuration is the telescopic grid that resolves mesoscale features across a substantial
fraction of the Northeast Pacific with highest grid refinement near the U.S. West Coast pole of the grid (Fig. 1b). At the same
110 time, the model simulates the circulation of the entire Pacific, avoiding the need to provide lateral boundary conditions except
at a few places in the Southern Ocean, i.e., more than 9000 kilometers away from the analysis domain.

We run two simulations with different carbon forcings. The first one corresponds to the simulation used by Desmet et al.
(2022) and consists of a hindcast simulation (HCast) from 1979 through 2019, where atmospheric pCO_2 is prescribed to
increase according to observations (Landschützer et al., 2020), and where the DIC concentration at the lateral southern open
115 boundary of the model is transient, but does not include interannual variability. Our HCast simulation uses slightly different
initial conditions than employed by Desmet et al. (2022) as a result of a change in the forcing used for the model spin up. While
Desmet et al. (2022) used daily fields from the year 1979 as the forcing for the spin up, we use a normal year forcing (apart
from atmospheric CO_2, which is transient). The normal year forcing is created by adding daily anomalies of the year 2001
to the climatological mean surface fields of wind stress, short and long-wave radiations, and freshwater fluxes derived from
120 ERA-5 (Hersbach et al., 2020; Copernicus Climate Change Service (C3S), 2017). The second simulation is a control simulation
(CCons), where we kept the long-term mean atmospheric pCO_2 and DIC concentration at the lateral southern boundary at the
1979 levels by linearly detrending them. This simulation was also run for the years 1979 through 2019. We discard the first
five years and then use daily mean outputs from 1984 to 2019 for both simulations for our analysis of the extreme events. The
hydrogen ion concentration ([H^+], at the total scale) and the saturation state of aragonite (Ω_A) are computed offline using the
125 MOCSY 2.0 routine as described in Desmet et al. (2022).

We divide the Northeast Pacific region (28°-62°N; 105°-155°W) into a total of four regions (Fig. 1a). Two are coastal regions
extending up to 300 km off the coast, namely the CCS (28°- 46.5°N) and the Alaskan Coastal Region (ACR; north of 46.5°N).

The choice of 300 km reflects on the one hand the average width of the nearshore band of high particulate organic carbon concentrations (Amos et al., 2019), and on the other hand the boundary inshore of which the majority of westward propagating

130   mesoscale eddies tend to form (Nagai et al., 2015; Chenillat et al., 2016; Amos et al., 2019). The other two regions are open ocean regions with the first one denoted as the "Offshore Northeast Pacific" (ONP), impacted by mesoscale eddies that originate from the nearshore regions and propagate all the way into this open ocean region. The second is the Central Northeast Pacific (CNP) that shows no evidence of this coastal imprint. We delineate the ONP and CNP regions by computing the eddy fronts at 100 m and 200 m, respectively and then taking the average of the two (see section 2.4 below for further details).
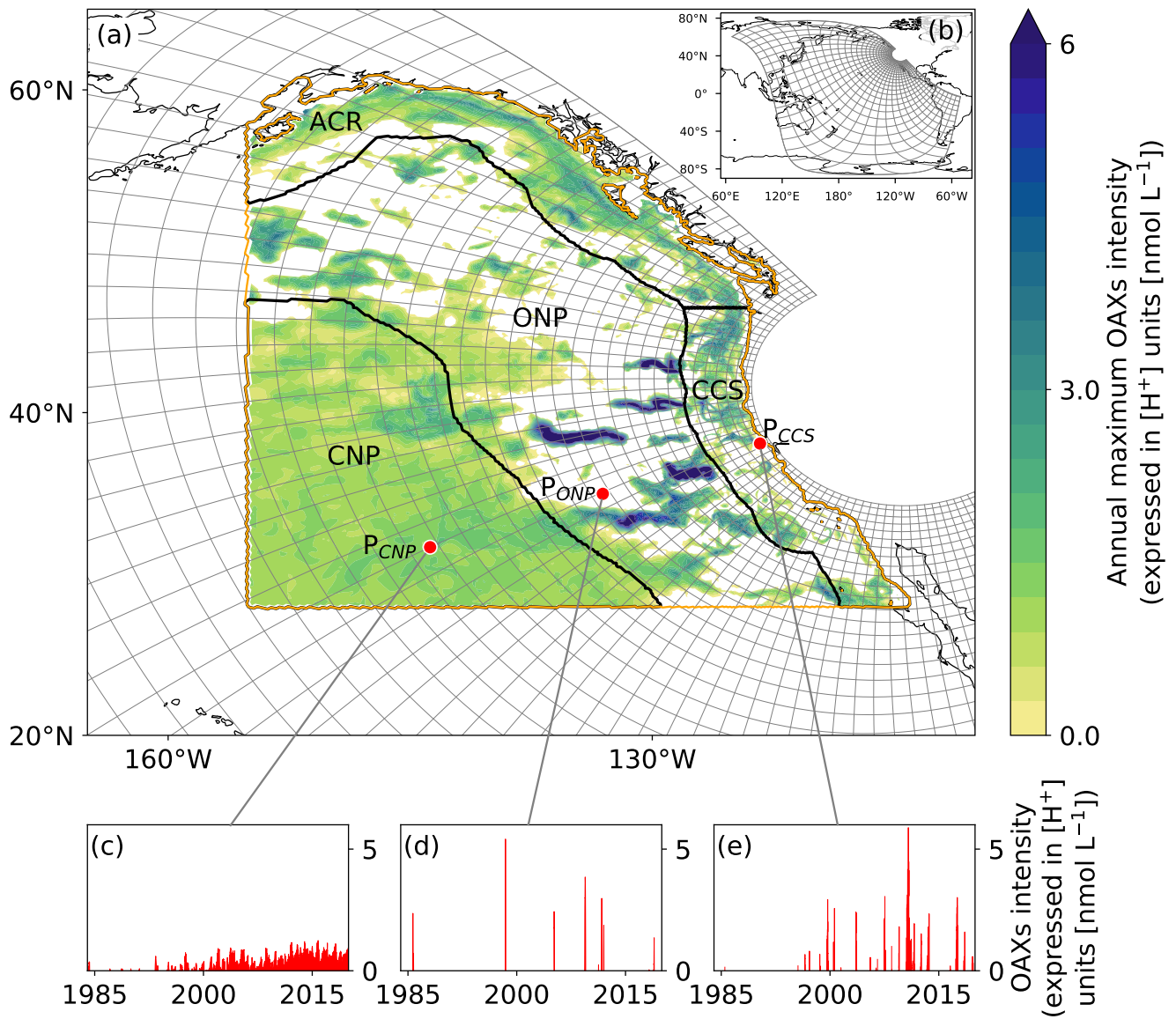
Figure 1. Map of the analysis domain and the selected subregions, and key properties of the diagnosed OAX. (a) Map of the Northeast Pacific with the telescopic grid of the model plotted in grey for every 10th grid cell. The black contours delimit the four selected subregions, i.e., the two coastal regions inshore of 300 km, namely the Alaskan Coastal Region (ACR) and the California Current System (CCS), and the two open ocean regions, i.e., the Offshore Northeast Pacific (ONP) and the Central Northeast Pacific (CNP). The domain of analysis is denoted by the orange contour line. The annual maximum intensity of the simulated OAXs in year 2014 at 100 m depth is plotted on top. White regions indicate that no OAX occurred in that year at this depth. (b) Map of the whole ROMS-BEC telescopic grid, plotted for every 20th grid cell. (c-e) Time series of [H$^+$] intensity at 100 m depth at the three locations depicted by red points in (a), i.e., (left) P$_{CNP}$ in the CNP region (31.66°N-143.77°W), (middle) P$_{ONP}$ in the ONP region (34.97°N-133.07°W), and (right) P$_{CCS}$ in the CCS (38.08°N-123.32°W).

2.2 Model evaluation

A thorough evaluation of the climatological distribution of key physical and carbon variables simulated in the HCast was provided by Desmet et al. (2022). This evaluation as well as that of the simulated daily surface variability gave excellent results, except for a tendency of the model to produce too low pH and Ω_A levels in the thermocline of the CCS. Although our HCast simulation is not numerically equivalent to the simulation employed by Desmet et al. (2022) owing to the different initial conditions (cf. Section 2.1), they present very similar evaluation results (not shown). Here we further evaluate the surface OA trends in pH and Ω_A of the model against observations (Table 1).

We first evaluate regionally averaged surface pH trends in the North Pacific against trends derived from SOCATv2 data (Lauvset et al., 2015) (Table 1). For better comparison, we spatially average surface pH over the biomes used in Lauvset et al. (2015) and then compute the linear trend on the spatially averaged time series. The modeled surface pH in the subtropical North Pacific decreases by 0.015 per decade from 1981 to 2011, which is within the range of the observed trend of -0.016 $\pm$ 0.002 decade^{-1} (Lauvset et al., 2015). The model's trend of -0.016 pH unit decade^{-1} from 1991 to 2011 in the subpolar North Pacific, although overestimated compared to observations, is also within the range of the observed trend of -0.013 $\pm$ 0.005 decade^{-1} (Lauvset et al., 2015).

Table 1. Linear trends in pH and Ω_A (per decade) for the two north Pacific biomes used in Lauvset et al. (2015) (subtropical and subpolar) and six stations (line P stations and ALOHA; see Appendix Fig. B1). Given are the modeled and observed trends, together with their two standard deviation credible intervals (95 % CrI).

Location	Time period	ROMS-BEC		Observations		References
		pH unit.decade^{-1}	Ω_A unit.decade^{-1}	pH unit.decade^{-1}	Ω_A unit.decade^{-1}	
i) Regional average						
Subtropical north Pacific	1981-2011	-0.0148 $\pm$ 0.0003	-	-0.016 $\pm$ 0.002	-	Lauvset et al. (2015)
Subpolar north Pacific	1991-2011	-0.0161 $\pm$ 0.0008	-	-0.013 $\pm$ 0.005	-	Lauvset et al. (2015)
ii) Stations						
P4	1990-2019	-0.0166 $\pm$ 0.0007	-0.057 $\pm$ 0.005	-0.011 $\pm$ 0.014	-0.04 $\pm$ 0.06	Franco et al. (2021)
P12	Feb. 1992-Jun. 2019	-0.0204 $\pm$ 0.0006	-0.080 $\pm$ 0.006	-0.016 $\pm$ 0.006	-0.06 $\pm$ 0.04	Franco et al. (2021)
P16	May 1990-Mar. 2018	-0.0200 $\pm$ 0.0006	-0.083 $\pm$ 0.007	-0.017 $\pm$ 0.008	-0.08 $\pm$ 0.04	Franco et al. (2021)
P20	1990-2019	-0.0180 $\pm$ 0.0005	-0.051 $\pm$ 0.005	-0.014 $\pm$ 0.006	-0.04 $\pm$ 0.04	Franco et al. (2021)
P26	1990-2019	-0.0180 $\pm$ 0.0005	-0.048 $\pm$ 0.005	-0.013 $\pm$ 0.004	-0.04 $\pm$ 0.02	Franco et al. (2021)
ALOHA	1988-2012	-0.0161 $\pm$ 0.0003	-0.090 $\pm$ 0.002	-0.016 $\pm$ 0.001	-0.084 $\pm$ 0.011	Bates et al. (2014)

We additionally evaluate our model simulated pH and Ω_A surface trends against time series data collected at station ALOHA (Bates et al., 2014), as well as against the line P time series (Franco et al., 2021). All the simulated trends are within the range of observed trends, except the pH trend at station P26 (Table 1). The average modeled surface pH (Ω_A) trend across the five line P stations is -0.019 decade^{-1} (-0.06 decade^{-1}) against -0.014 decade^{-1} (-0.05 decade^{-1}) in Franco et al. (2021).

While the evaluation of subsurface pH and Ω_A trends is not yet possible given the lack of long-term time series observations, we evaluate the simulated subsurface trends in dissolved inorganic carbon down to about 300 m depth against observations

derived from the line P time series (Appendix Fig. B2; Franco et al., 2021). The simulated dissolved inorganic carbon trends (DIC is normalized to a salinity of 33 psu) in the subsurface of line P stations are in the range of observed trends (Appendix Fig. B2). However, the model tends to have larger trends than suggested by the observations. In intermediate waters (150-300 m depth), simulated DIC trends are 2 % larger than the upper bound of observed trends in open ocean stations, and 15 % larger in the coastal station P4 (Appendix Fig. B2). We further discuss the implications of this discrepancy in the caveat section 4.4.

Overall, although subsurface trends in dissolved inorganic carbon tend to be overestimated, our model simulates pH and Ω_A surface trends within the range of the trends that have been observed during the last four decades, giving us confidence in the analysis of the progression of acidity extreme events.

2.3   Ocean acidity extremes (OAX)

We define ocean acidity extreme events (OAXs) as temporally connected grid cells, for which [H⁺] exceeds the 99th percentile of temporally aggregated daily [H⁺] from 1984 to 2019 at a given location (similar as in Gruber et al., 2021). To determine the 99th percentile threshold, we used the CCons simulation where the long-term mean atmospheric CO_2 was kept at the 1979's levels. In other words, we used a fixed baseline approach where the initial conditions of the late 1970s were used as the reference period. This choice of a reference period is somewhat arbitrary, but the late 1970s/early 1980s represent for many oceanographic parameters the first period for which we have global-scale observation based estimates (see e.g., Ma et al. (2023)). This temporally fixed threshold was then used to detect OAXs in both the CCons and HCast simulations. We focus our analysis on OAX occurring in the upper 250 m of the water column.

We derive three local metrics, namely (i) yearly extreme days (in days; number of days per year above the 99th percentile of [H⁺]), (ii) annual mean event duration (in days; the average number of consecutive days above the 99th percentile of single events within a year) and (iii) annual maximum intensity (in nmol L⁻¹; maximum [H⁺] anomaly with respect to the percentile threshold). These metrics are computed at three depths, i.e., the surface layer in direct interaction with the atmosphere, and two subsurface layers, namely 100 m corresponding to the transition from the euphotic zone to the twilight zone, and 200 m, corresponding to the upper thermocline. Note that while the truncation of extremes between years alters the results for duration, it allows for the calculation of annual extreme-event characteristics. We additionally derive an integrative metric, namely the annual mean volume fraction of OAX (in %; the average fraction of the daily volume of grid cells with [H⁺] above the 99th percentile relative to the total volume extending from 0 to 250 m depth), computed separately for each of the four regions of the Northeast Pacific depicted in Fig. 1a (ACR, CCS, ONP and CNP) and three depth bins (0-50 m, 50-100 m and 100-250 m). Additionally, we compute in each of these regions the fraction of the volume of the [H⁺] extremes that is undersaturated with regard to aragonite ($\Omega_A < 1$) at the time of the extreme. Within the OAX with undersaturated conditions, we further identify those that are supersaturated ($\Omega_A \geq 1$) in the CCons simulation. We refer to this last fraction as the fraction of newly undersaturated OAXs.

2.4 Return periods, time of emergence (ToE) and eddy front

We characterize the return periods of different [H$^+$] intensity levels using the generalized extreme value distribution G (Coles, 2001):

$$G(z) = \exp\left[-\left(1 + \xi\frac{z-\mu}{\sigma}\right)^{-\frac{1}{\xi}}\right], \quad \text{for } 1 + \xi\frac{z-\mu}{\sigma} > 0,$$

where μ, σ, and ξ are the location, scale, and shape parameters, respectively. We extract the annual maxima [H$^+$] at each grid cell and fit G to the annual maximum data for the 1984-1998 and 2005-2019 periods respectively using the *stats.genextreme* function from Scipy. We then compute at each location the return periods (in years) for 24 discrete return intensity levels ranging from 0.05 to 6 nmol L^{-1}. We focus on return periods shorter than a century and set all longer return periods to 200 years prior to computing the spatial median, 40th, and 60th percentile return periods within the ACR, CCS, ONP, and CNP regions at the surface and at 100 m and 200 m depth. The method is found to be robust to the number of data points to which G is fitted, i.e., 15 datapoints for each period in our study, given the small standard deviation (1.4 years) of the return periods computed for the CCons scenario on 15, 20, and 25 years (respectively 15, 20, and 25 datapoints; Appendix Fig. B3).

We compute the time of emergence (ToE) as a measure of the time it takes for the linear long-term trend signal to exceed the 99th percentile threshold used to detect OAX. We first compute at each individual grid cell a linear regression from the daily [H$^+$] data from 1984 through 2019 from the HCast scenario, assuming the trend signal to be linear over this period. We then calculate the number of years after 1979 when this linear trend exceeds the 99th percentile threshold computed from the CCons scenario daily data from 1984 to 2019. This is done at each location at the surface and at 100 m and 200 m depths. We refer to as "near permanent OAX" when emergence has occurred, i.e., when the linear long-term trend signal has exceeded the 99th percentile threshold used to detect OAX.

At both 100 m and 200 m depth we define an eddy front based on the westward extent of detected eddy-driven OAXs in Desmet et al. (2022). This eddy front measures the farthest distance from the coast at which eddy-induced variability significantly alters the [H$^+$] threshold (99th) value in our simulation. Such alteration occurs when eddy-induced variability accounts for more than 1 % of the time period at a given location, in which case the threshold depends on the [H$^+$] carried by mesoscale eddies rather than background variations at that location (Appendix Fig. A1). Further offshore of this front, the threshold of the offshore regime is not affected anymore by the mesoscale imprint of nearshore conditions. Detailed methodology on the calculation of the depth-dependent eddy front can be found in Appendix A.

3 Results

3.1 Progression of OAX in the Northeast Pacific

Between 1984 and 2019, the annual mean volume fraction characterized by extreme [H$^+$] conditions (OAX) in the upper 250 m increases manifold, yet spatially varied across the Northeast Pacific (Fig. 2). In the upper 50 m, this volume fraction increases from a few percent in the early 1980s to around 40 % in the two coastal regions (Fig. 2a,d), and to about 85 % in the open

ocean regions (Fig. 2g,j), representing a between 8 and 15-fold increase over the 36 years of our simulation. In the 50-100 m depth range, the regional differences are even larger. While the Central Northeast Pacific (CNP) approaches permanent extreme conditions (OAX volume fraction > 95 % on average during the last 5 years), the other regions experience a more

220 modest increase (Fig. 2b,e,h,k). This strong regional difference persists in the 100-250 m depth range, with the CNP region experiencing an increase to a volume fraction of OAX of more than 50 %, while the volume fraction in the adjacent ONP open ocean region increases to only about 10 %, similar to the changes seen in the two coastal regions (Fig. 2c,f,i,l). Furthermore, the temporal progression differs across regions. The increase is mainly linear in the surface layer, while the subsurface (i.e., below 50 m depth) experiences more abrupt transitions and stronger year-to-year variability. Striking is the step increase in

225 OAX in the subsurface layers of the two coastal regions around the year 1995 (Fig. 2b,c,e,f). This is also seen in the open ocean regions (Fig. 2h,k). The strongest year-to-year variability is found in the 100-250 m range of the two coastal regions, with a near collapse of the OAX volume fraction in the CCS and ACR in 2015, concomitant with the strong El Niño 2014/16 (Fig. 2c,f).
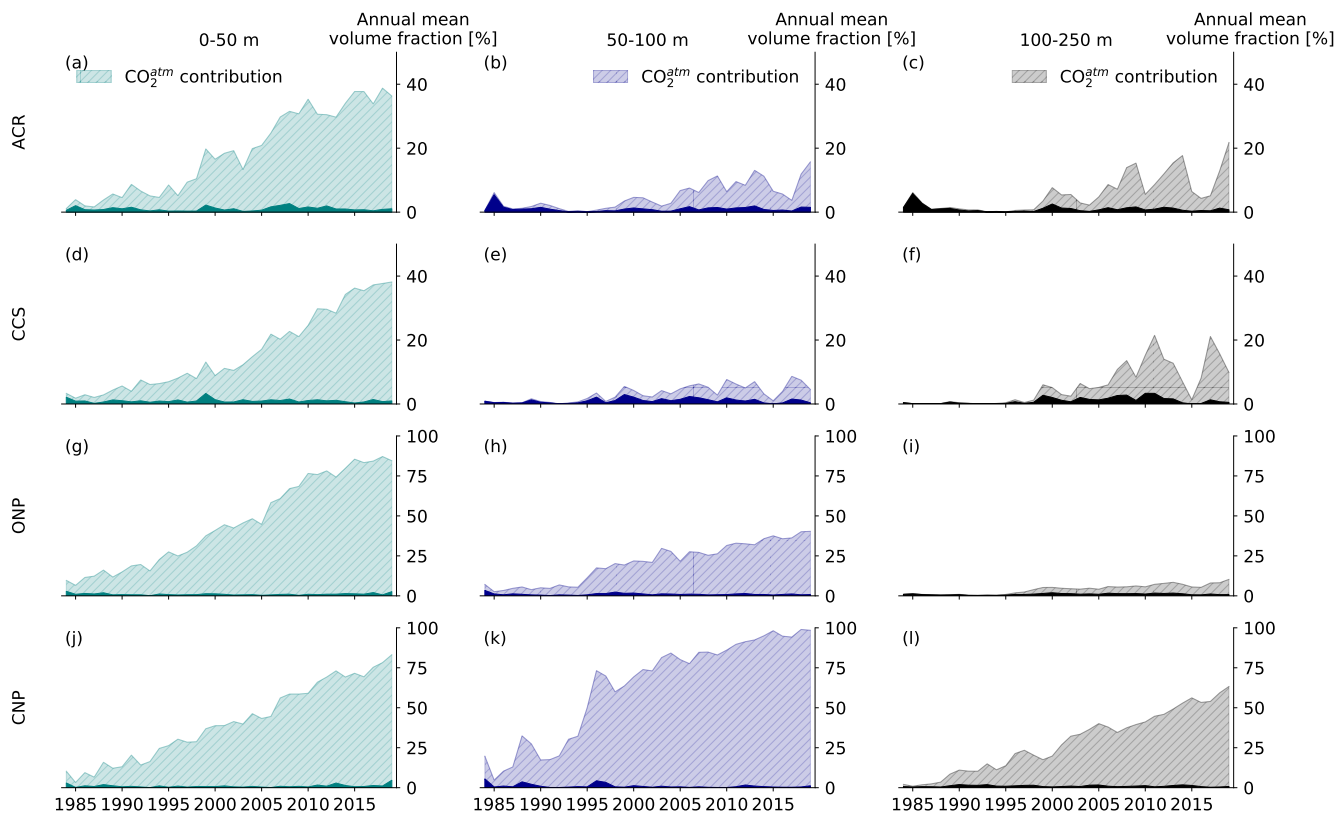
Figure 2. Time series of the annual mean volume fraction characterized by [H$^+$] extremes (OAX) for the four different regions of the Northeast Pacific shown in Fig. 1a (rows) and three different depth sections (from left to right: 0-50 m, 50-100 m and 100-250 m depth). Dark and light colours depict the OAX volume fraction in the CCons and HCast scenario, respectively, with the difference between the two denoting the contribution of the rise in atmospheric CO_2 to the OAX volume fraction from the HCast scenario (CO_2^{atm} contribution, hatched area). Note the different scales of the top two (0-50 %) and bottom two rows (0-100 %).

Many of the OAX below the top 50 m, and especially those in the coastal regions are also characterized by undersaturated
230 (corrosive) conditions with regard to the $CaCO_3$ mineral aragonite, i.e., have $\Omega_A < 1$ (Table 2). This joint stress from extremely low pH and corrosive conditions is expected to be particularly harmful for ocean organisms that form shells out of aragonite such as pteropods (Bednaršek et al., 2014; Feely et al., 2018). While such corrosive conditions in OAX are rare in the upper 50 m of the ocean, between 66 % and 100 % of the OAX events are corrosive below 50 m in the two coastal regions. Also in the ONP below 100 m, the majority (60 %) of the OAX have such corrosive conditions (Table 2). While the majority of these
235 events would have been corrosive even in the absence of any increase in atmospheric CO_2 in the 100 to 250 depth layer, about an eighth (CCS) to a third (ACR) of the corrosive OAX between 50 and 100 m depth in the two coastal regions have become corrosive over the course of the 41 years of our simulation (Table 2). There, 10 % and 21 %, respectively, of the volume of OAX has become undersaturated, while these waters would have stayed supersaturated without the increase in atmospheric

CO_2. In contrast to the subsurface waters in the ACR, CCS, and ONP regions, the OAX in the subsurface waters of the CNP remain supersaturated.

These differences in corrosiveness of the OAX reflect the distribution of the climatological saturation horizon (depth level where $\Omega_A = 1$) and how this horizon shoals in response to the invasion of anthropogenic CO_2. With the atmospheric CO_2 kept at the 1979 level, this horizon sits below 300 m in the CNP and ONP regions, but shoals to less than 60 m in the nearshore coastal regions. Still, the saturation horizon sits below 100 m in more than 80 % of the coastal areas (Appendix Fig. B4). With the increase in atmospheric CO_2 this horizon shoals by 45 m on average in coastal areas, bringing the saturation horizon into the top 100 m, leading to many additional corrosive OAX.

Table 2. Fraction (in %) of the OAX volume that is characterized by undersaturated conditions with regard to aragonite averaged over 1984-2019 for the four different regions of the Northeast Pacific shown in Fig. 1a and for three different depth layers. Numbers in the "Ω_A newly < 1" column give the fraction of the OAX volume that is newly undersaturated with regard to aragonite. This is computed by identifying the fraction of the OAX volume that is undersaturated in the HCast simulation but supersaturated in the CCons simulation where atmospheric CO_2 was kept at its 1979's value.

	0-50 m		50-100 m		100-250 m	
	Ω_A newly < 1	$\Omega_A < 1$	Ω_A newly < 1	$\Omega_A < 1$	Ω_A newly < 1	$\Omega_A < 1$
Alaskan Coastal Region (ACR)	<1	1	21	66	4	100
California Current System (CCS)	<1	2	10	81	1	100
Offshore Northeast Pacific (ONP)	$\ll 1$	$\ll 1$	1	4	5	60
Central Northeast Pacific (CNP)	0	0	0	0	<1	1

3.2 Role of rise in atmospheric CO_2

The strong increase in the OAX with time is almost entirely attributable to the increase in atmospheric CO_2 (CO_2^{atm} contribution in Fig. 2). If atmospheric CO_2 was held at the 1979 levels, the volume of OAX would have exhibited no significant trend (dark colored areas), but only would have fluctuated from year-to-year at a level of a few percent in all regions and depth layers. Concretely, depending on the depth layer and region, the fraction of the volume occupied by OAXs in the last 15 years of the hindcast is 4 to 160-fold larger than in the CCons simulation, where atmospheric CO_2 did not increase (Fig. 2).

In order to assess the impact of the rise in atmospheric CO_2 in more detail and to also diagnose its impact on the duration and the annual maximum intensity of the OAX, we analyze these metrics as a function of atmospheric CO_2 rather than as a function of time (Fig. 3). This permits to scale the various metrics as a function of the main driver of change. We thereby combine the two coastal and two open ocean regions.
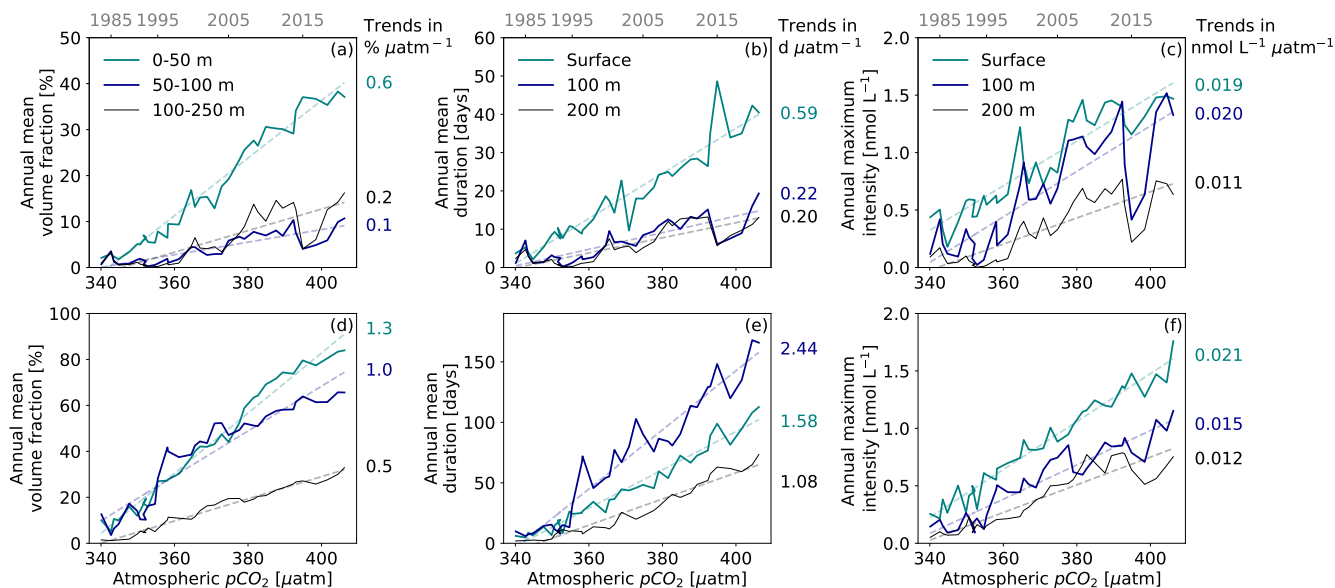
Figure 3. OAX characteristics as a function of atmospheric CO_2 between 1984 and 2019 in the (top row) two coastal and (bottom row) two open ocean regions of the Northeast Pacific analysis domain. (a,d) Annual mean OAX volume fraction in three different depth layers (0-50 m, 50-100 m and 100-250 m depth). (b,e) Annual mean event duration (days) and (c,f) annual maximum intensity (nmol L^{-1}) at surface (cyan), 100 m (darkblue) and 200 m (black) depth. In all panels, the simulated OAX characteristics are plotted against the yearly averaged atmospheric pCO$_2$ over the Northeast Pacific domain. Corresponding years are indicated at the top. Linear regressions (r^2 > 0.7) are plotted in each panel and the associated rates of increase (per μatm) are given.

On average across the entire Northeast Pacific, OAXs occupy an additional 6.3 % of the upper 250 m depth, last 10.2 days longer, and are 0.16 nmol L^{-1} ($\approx$ -0.006 pH units) more intense for every additional 10 μatm of CO_2 in the atmosphere. Near the surface, the increase in OAX volume fraction linearly follows the atmospheric CO_2 rise in both coastal and open ocean

260 regions (r^2 >0.96), with a rate of change in the open ocean regions that is twice as large as that in the coastal regions, i.e., 1.3 % versus 0.6 % μatm^{-1} (Fig. 3a,d). The increase rate decreases substantially below 50 m in the coastal regions (Fig. 3a) and below 100 m depth in the open ocean regions (Fig. 3d). Between 50 and 100 m depth, the offshore OAX volume fraction abruptly increases at about 355 μatm, corresponding to the early step increase in Fig. 2h,k.

Similar near-linear relationships with the rise in atmospheric CO_2 are found for the annual mean duration (Fig. 3b,e) and for

265 the annual maximum intensity of the OAX (Fig. 3c,f). In the coastal regions, the duration increases twice as fast at the surface than in the subsurface (0.59 and 0.21 days μatm^{-1} respectively; Fig. 3b). While the annual mean duration of OAX at the surface is ∼7 days under atmospheric CO_2 levels of 1984-1998 (∼351 μatm), it is nearly 4 times longer, i.e., about 30 days under atmospheric pCO$_2$ levels of 2005-2019 (∼390 μatm). At depth, the lower rate of increase leads to durations toward the end of the simulations of around 10 days (Fig. 3b).

270 In the open ocean regions, the duration of the OAX are first of all much longer than in the coastal regions, and also increase faster (Fig. 3e). At the surface, the rate of increase is three times larger than in the coastal regions (∼1.58 days μatm^{-1}),

increasing the duration of an [H$^+$] extreme from $\sim$16 days in the first 15 years of the hindcast to more than 75 days in the last 15 years. The rate of increase in the open ocean regions is largest at 100 m, being about 50 % larger than that at the surface, and more than twice as large as at 200 m.

275   The annual maximum intensity of OAX also increases with increasing atmospheric CO_2 throughout the Northeast Pacific, but in contrast to the other metrics, there are fewer differences between regions and between different depths (Fig. 3c,f). In the coastal regions, the maximum intensity doubles at the surface between 1984-1998 and 2005-2019, increasing from values around 0.5 nmol L^{-1} to more than 1 nmol L^{-1}. This equates to an oceanic pH change of about -0.022. Down to 100 m depth in coastal regions and in the surface of open ocean regions, the intensities increase at nearly the same rate than simulated at the

280 surface of coastal regions. At 200 m depth however, and in the subsurface of open ocean regions, the increase is about 35 % slower and the annual maximum intensities also remain lower (around 0.1 to 0.3 nmol L^{-1} in the 1980s, increasing to values between 0.5 and 1 nmol L^{-1} in the 2005-2019 period).

    By contrasting the above results (Fig. 3; HCast simulation) with those from the CCons simulation, we can attribute the trends in the annual mean duration and annual maximum intensity to the rise in atmospheric CO_2. This comparison shows that, as

285 was the case for the volume of OAX, the increases in duration and maximum intensity are almost exclusively driven by the increase in atmospheric CO_2 (not shown).

3.3   Heterogeneous distribution of OAX intensities

The highly spatially aggregated data in Fig. 3c,f hide the existence of substantial spatial differences in the distribution of the annual maximum intensities, especially at depth (Fig. 4). While the annual maximum intensities and their changes with time

290 tend to be spatially relatively uniform at the surface, these intensities and changes are spatially very heterogeneous at depth. Particularly striking is the presence of a front at about 1500 km from the westcoast of the Americas, separating waters with very high maximum intensities of OAX to the east from waters with relatively low maximum intensities to the west. In fact, some of the highest maximum intensities are found just to the east of this front. As shown by Desmet et al. (2022), this pattern of OAX intensities is the consequence of what they called "Large, Long, and Propagating" (LLP) OAX. These LLP OAX

295 events originate near the coast of the Americas and then propagate for months and years westward. They harbor rather intense extremes as a consequence of encapsulating low pH and low Ω_A waters during their formations near the coast, by isolating the extreme conditions within them owing to their rotation, and by partially enhancing these OAX conditions throughout their lifetime by enhanced export production and remineralization at depth, increasing [H$^+$].

    In our model simulations, these LLP OAXs dissipate at this intensity front, causing a very rapid drop-off of the maximum

300 intensity to the west of it. This drop-off is located a few hundred kilometers closer to the shore at 100 m depth compared to the situation at 200 m depth. The presence of this front was the reason for separating the open ocean region into two sub-regions, i.e., the ONP and CNP (see section 2.4 and in Appendix A, whereby we used the average position of the front at 100 and 200 m to delineate these two regions). In the open ocean regions east of this front, i.e., in the ONP, the map reveals a highly patchy distribution of high maximum intensities, reflecting the pathways of the episodic high LLP events. Inside these LLP, the annual

305 intensities can reach values of well above 5 nmol L^{-1}. In contrast, the annual maximum intensities to the west of this front

are generally less than 1 nmol L^{-1}. The pattern of the increase of the maximum intensities follows the spatial distribution of average annual maximum intensity seen in both 15 years periods (contrast panels f and i with panels d,e and g,h, respectively in Fig. 4), with increases in many places of up to 3 nmol L^{-1}. This implies that the lines for the open ocean regions in Fig. 3f represent an average of two sub-regions with distinctly different OAX intensities and changes thereof.

310
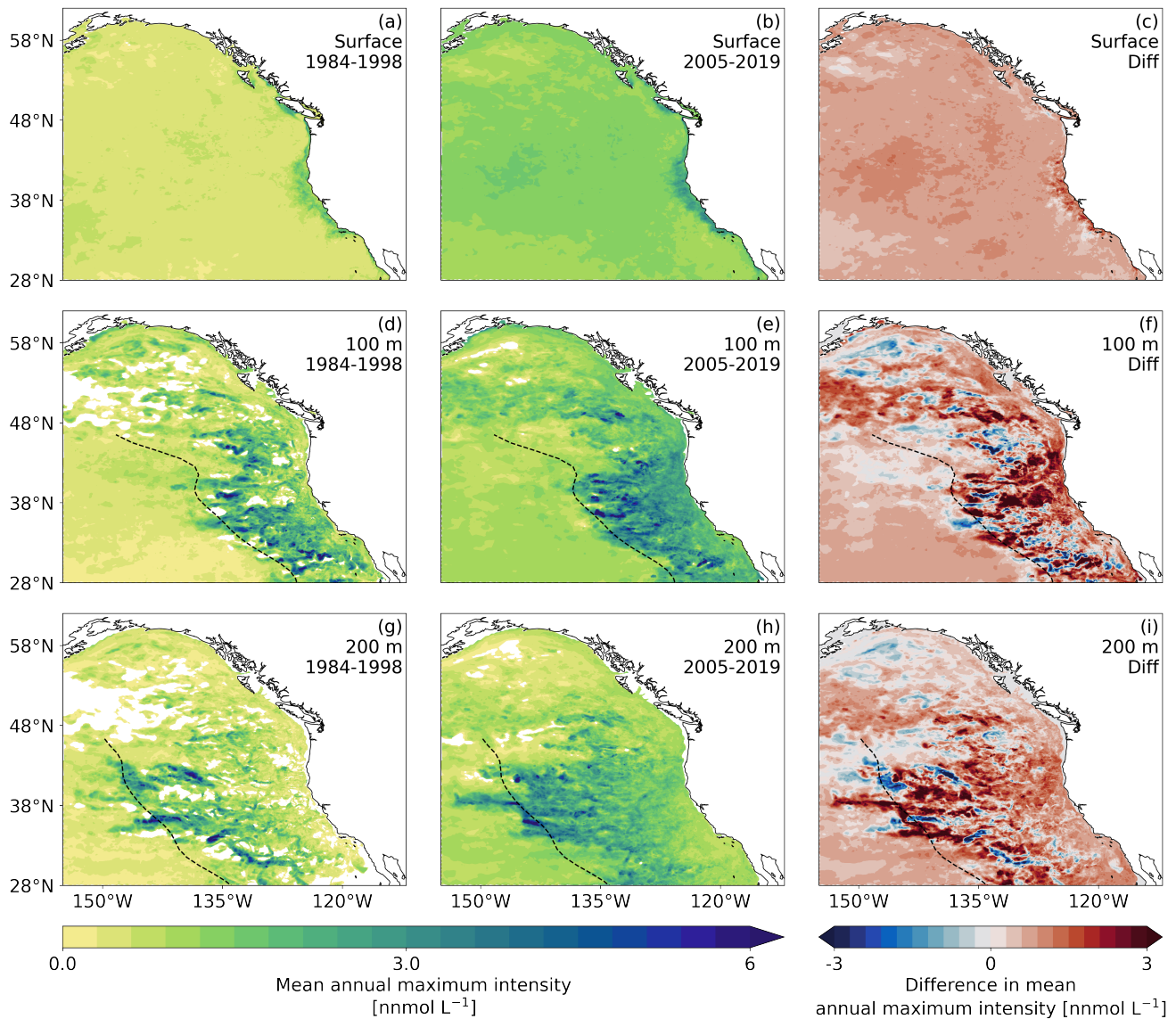
Figure 4. Maps of the average annual maximum intensity of [H$^+$] extremes for (left column) the period 1984-1998, (middle column) 2005-2019, and (right column) difference between the two periods. (a)-(c) Average conditions and difference for the surface layer. (d)-(f) As for (a)-(c) but for the a depth of 100 m, and (g)-(i), as for (a)-(c), but for a depth of 200 m. For the average, only years with extremes are taken into account. White areas depict areas that did not experience any extremes over the respective decade. The black dashed lines depict the front formed by the maximum extent of the westward propagating eddies at 100 and 200 m, respectively.

3.4 Change in return intensity

The rapid increase in intensity of [H⁺] extremes causes between the first and last 15 years of the hindcast a substantial increase in the [H⁺] intensity associated with a given return period (Fig. 5). Intensity levels that were rare to unlikely from 1984 to 1998 have become frequent in the last 15 years. For instance, an intensity of 1 nmol L⁻¹ (∼-0.020 pH unit) was rare at 100 m depth in the CCS (one in 13.3 years event) but occurs every second year in the last 15 years (one in 1.7 years event; Fig. 5b). Similarly, at 100 m depth in the CNP, such an intensity occurs once in a hundred years based on the data of the first 15 years. 20 years later between 2005 and 2019, such an event is estimated to occur every second year (one in 2.2 years event; Fig. 5e). Changes in the return period of high intensities are also large. An intensity of 4 nmol L⁻¹ (∼-0.087 pH unit) would not occur in a hundred years at 100 m depth based on the data of the first 15 years while it represents a one in 19.2 (27.1) years event in the CCS (ONP) in the last 15 years (Fig. 5b,e).
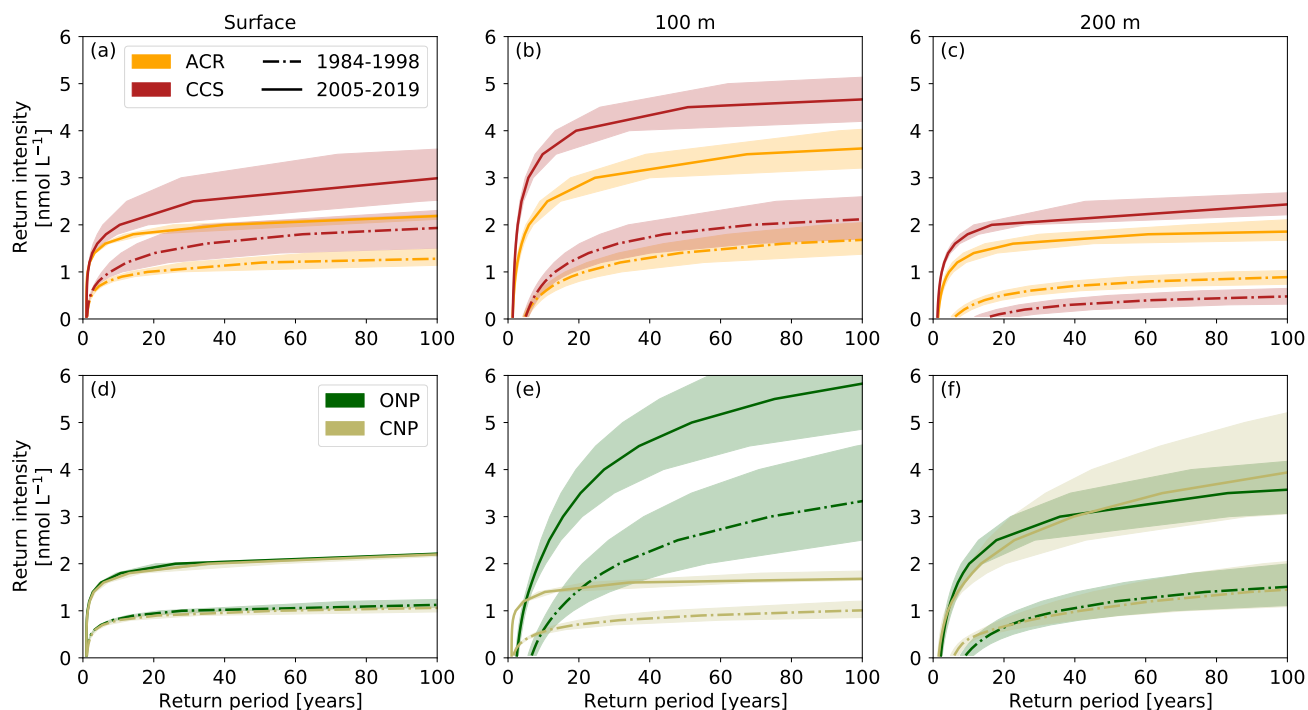
Figure 5. Return intensity (in nmol L⁻¹) as a function of the return period (in years) for the HCast scenario at the (a) surface, (b) 100 m, and (c) 200 m depth in the (top) ACR and CCS, and (bottom) ONP and CNP regions, for two different time periods, respectively 1984-1998 (dashdot) and 2005-2019 (solid). The line represents the median and the shading the 40th-60th percentile interval based on the spatial variability within each region.

As the other metrics, the return intensities as well as the magnitude of their change vary spatially and with depth. At the surface, the changes in the return intensity tend to be smaller than in the subsurface, and similar between regions, as they are for the intensity itself (Fig. 4c and 5a,d). The largest changes in return intensity occur at 100 m depth, in particular in inshore

areas and in the ONP region where the one in ten years return intensity increases by 2.07 nmol L^{-1} (~-0.048 pH unit) on average (from 0.63 to 2.71 nmol L^{-1}; Fig. 5b,e). Finally, some regions exhibit substantial spatial variability in the return periods associated to given return intensity (Fig. 5). The largest spatial variability is found at 100 m depth in the ONP region, matching the strong variance of OAX maximum intensity in this region (Fig. 4d,e and 5e).

Overall, the rate of change of OAXs and their characteristics in response to the increase in atmospheric CO_2 varies in space and depth (Fig. 2, 3, 4 and 5). While the surface response is rather linear in time and homogeneous in space, the subsurface response is more variable and depends on the marine environment being an inshore/offshore regime or an intermediate offshore regime with substantial coastal imprint from mesoscale eddies.

3.5   Rapid vs. delayed emergence of near permanent OAX

While the volume of OAX already revealed some substantial non-linear response to the rise in atmospheric CO_2 with abrupt onsets and rapid expansions (Fig. 2), the last metric of interest, i.e., the number of extreme days per year, shows the most striking pattern of abruptness (Fig. 6). The increase in yearly extreme days between the first and last 15 years of the hindcast shows sharp spatial transitions at all depths, but distributed heterogeneously in space, with large differences in the magnitude of the increase. The increases in the number of extremes days reach up to more than 200 days, leading to almost year-round OAXs towards the end of the hindcast in some locations (Fig. 6f).
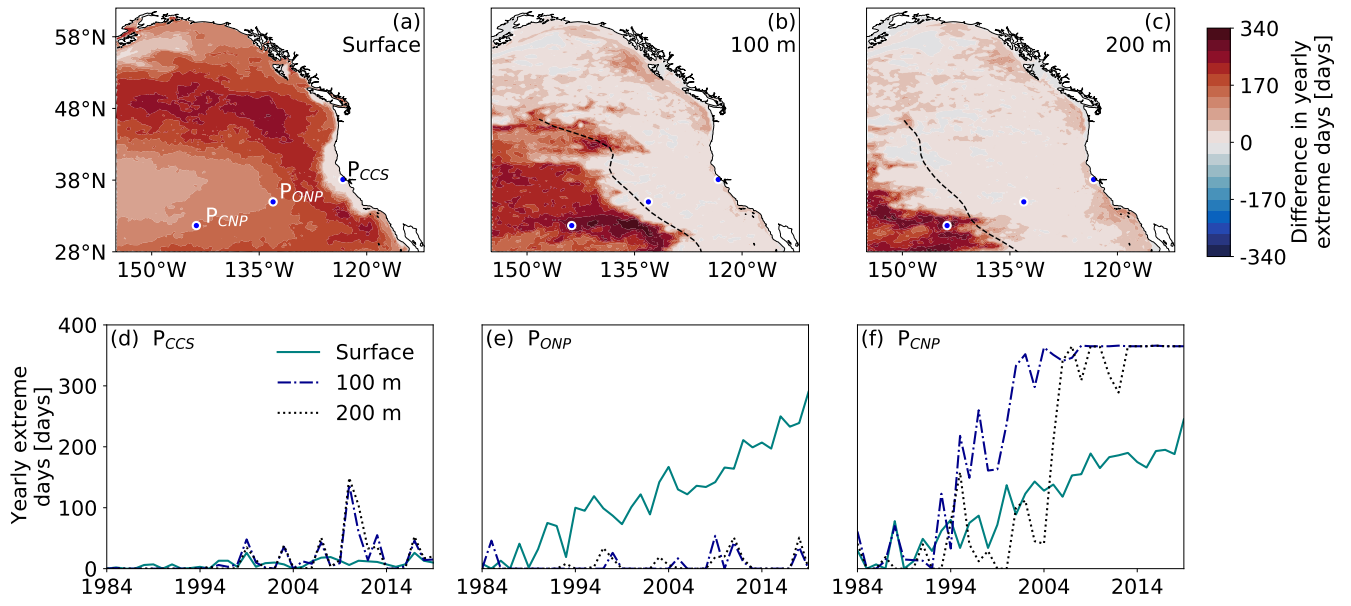
Figure 6. Spatiotemporal progression of the yearly [H$^+$] extreme days in the Northeast Pacific. (a) Map of the difference in yearly [H$^+$] extreme days between 2005-2019 and 1984-1998 in the HCast simulation at the surface; (b) as (a), but for 100 m depth; (c) as (a) but for 200 m depth. The three blue disks with white contours in each map denote the locations for the time series in panels (d) - (f), reflecting a location in the nearshore CCS (d), a location in the ONP region (e), and in the CNP region (f). The black dashed lines in (b) and (c) denote the location of the westward eddy propagation front.

340   The strongest step increases in the yearly number of extreme days occur in the subsurface of the CNP (Fig. 6d-f). In only two years (between 2004 and 2006), the yearly number of extreme days at 200 m at point P$_{CNP}$ jumps from ∼30 to more than 300 days (Fig. 6f). Similarly, at 100 m depth, the yearly number of extreme days jumps from ∼30 to 150 days in one year (1994-1995) and to more than 300 days 6 years later (2001). These local step responses are also seen in the OAX volume fraction of the 50-100 m depth layer of the CNP (Fig. 2k), although the step response tends to be masked by the aggregation that occurs when the volume fraction is computed. In contrast, no such step response occur during our analysis period in the

345   subsurface central CCS and ∼1000 km offshore (P$_{CCS}$ and P$_{ONP}$), where only a small increase in yearly extreme days is seen (Fig. 6). OAXs remain episodic even towards the end of the hindcast under elevated atmospheric CO$_2$ levels (Fig. 6d,e). At the surface, large increase in yearly extreme days is found in most areas but the coastal central CCS (Fig. 6a). Overall, the area experiencing large increases shrinks with depth. In the subsurface, the sharp spatial transition in the response coincides with

350   the front in annual maximum intensity and its change (Fig. 4d-i) described in section 3.1 as well as with the westward extent of eddy-driven OAXs, i.e., the eddy-propagation front (black dashed lines in Fig. 4 and 6).

The spatial pattern of the large vs. small increase in yearly extreme days is well reflected in the spatial distribution of the ToE (Fig. 7). The area experiencing near permanent OAX before the end of the hindcast (ToE ≤ 41 years) decreases with depth. At the surface, 88 % of the Northeast Pacific experience near permanent OAX in 2019 (Fig. 7a). Only the CCS and ACR

355 have a stronger surface [H⁺] variability than surface [H⁺] trend under increasing atmospheric CO_2 within the time frame of the hindcast. In the subsurface however, only 40 % and 15 % of the Northeast Pacific, at 100 m and 200 m depth respectively, experience near permanent OAX in 2019 (Fig. 7b,c). Both at 100 and 200 m depth, ToE less than ∼40 years are confined to the offshore regions that do not have an imprint from coastal variability, i.e., in the CNP west of the eddy front. At P_{CNP}, the ToE is as short as 18 years at 100 m depth, matching the early step response in yearly extreme days seen at that location (Fig. 6f).
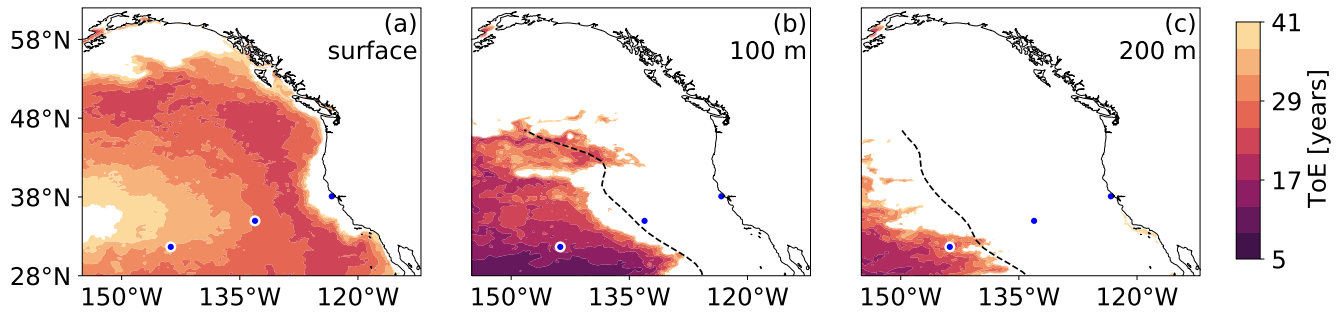
Figure 7. Maps of the Time of Emergence (ToE) of the yearly mean [H⁺] (long-term trend in [H⁺]) above the local [H⁺] threshold at (a) the surface, (b) 100 m depth, and (c) 200 m depth in the HCast simulation. White areas denote regions where the long-term trend does not exceed the threshold at the end of 2019 (i.e., ToE>41 years). The three blue disks with white contours in each map denote the locations where the time series in Fig. 1 and 6 were extracted. The black dashed lines denote the westward eddy propagation fronts.

4 Discussion

4.1 OAX increase in response to the rise in atmospheric CO_2

The increasing rates of the yearly number of extreme days, duration, and intensity of OAX with respect to increasing atmospheric pCO_2 found in our study are in the same order of magnitude than the ones estimated in previous OAX studies in the global ocean over the historical period 1861-2005 (Burger et al., 2020; Gruber et al., 2021). The similarity in the rates of
365 increase despite the different time frames of the two compared periods (145 years vs. 36 years) underlines the key role of atmospheric pCO_2 in OAX increase over time. Despite different models used and associated distinct resolutions, the surface increase rates in number of OAX days are similar between our study (3.7 days.μ atm⁻¹) and the study by Burger et al. (2020) (cf. Fig. 4a in their study). In the subsurface however, the increase rate in number of extreme days and OAX duration largely differs between the two studies. The increase in number of extreme days at 200 m depth is almost three times slower in our
370 study than in Burger et al. (2020) (cf. Fig. A1e of their study), and a similar difference is found for OAXs duration (cf. Fig. A1c,d in Burger et al., 2020). In subsurface waters, where mesoscale processes, such as eddies, largely contribute to broaden the distribution of [H⁺] (Appendix Fig. B6e,f), differences in OAX increase rate are more dependent on the model resolution than at the surface. In our high-resolution eddy-resolving study, broader distributions lead to thresholds more distinct from the

mean than in coarser resolution model that do not resolve mesoscale processes. This likely lead to the slower but more realistic subsurface increase in number of OAX days and OAX duration in our study with respect to increasing atmospheric pCO_2.

Emphasizing the rapidity of the changes in OAX is the drastic reduction in the return period of high intensities between the 1984-1998 and 2005-2019 periods. In less than 40 years, extremely rare ($\gg$100 years) high intensities become a one in less than 30 years event. Similarly, a strong reduction in the return periods of intense marine heatwaves is projected under global warming (Laufkötter et al., 2020). The rapidity of the change is further corroborated by the near permanency of OAXs that is reached in a large fraction of the upper 250 m of the Northeast Pacific within the time frame of our hindcast. The near permanency of extreme conditions has also been projected to occur between 2030 and 2050 for aragonite undersaturation events (absolute threshold) at the seafloor of the 10 km coastal CCS (Hauri et al., 2013a). From a mean duration of 16 days in 2010, those events are projected to reach near permanency in less than 40 years (Hauri et al., 2013a). In our study however, OAXs, defined based on a relative threshold, do not reach near permanency in the CCS given the strong natural variability of the region. This highlights the very different perspectives of using absolute versus relative thresholds to define extreme events.

When using a relative threshold and a fixed baseline to define OAX, the ratio of the long-term trend to local variability is key in determining the increase in OAX. Thus temporal changes in the variability can have a substantial influence on the evolution of the OAX. Such an increase in variability is actually expected as a consequence of ocean acidification (see also Burger et al., 2020), driven by the increase in the hydrogen ion concentration and a higher sensitivity to change. The variability can also change as a consequence of changes in weather and climate. In our simulations, the variability of $[H^+]$ increases in all surface regions and in the subsurface of the CCS, ONP, and CNP regions (Appendix Fig. B5). However, these increases in variability tend to contribute comparatively little to the overall increases in the OAX. We can estimate this contribution most easily in the regions where the $[H^+]$ distributions are Gaussian (e.g., at 100 m depth of P_{CCS}). There, the increase in variability increases the number of OAX days by a factor of 1.3, which is an order of magnitude smaller than the impact of the change in the mean state, as this leads to a 14-fold increase. Similarly, the maximum OAX intensity would increase by only 2 % from the change in variability, versus the intensity increases by 82 % from the change in mean state.

4.2 Spatial heterogeneity in OAX increase

Although rapid, changes in OAX are spatially heterogeneous in the Northeast Pacific. While OA trends are of similar magnitude between the studied regions and depths, differences in types and magnitudes of the marine environment's natural variability lead to varying increase in OAX (Fig. 8). The relatively slow and progressive increase in OAX in the nearshore central CCS can be explained by the strong natural variability of the region. The amplitude of surface $[H^+]$ variability is about six times larger than the magnitude of the OA trends from 1984 to 2019 (Appendix Fig. B6a). The same variability versus trend pattern and subsequent OAX response holds for the subsurface. While it is beyond the scope of this work to assess the mechanisms driving the strong year-to-year variability in OAXs in the coastal regions (Section 3.1), this variability largely correlates with the El-Niño-Southern-Oscillation, particularly impacting OAX in coastal regions of the Northeast Pacific, as shown in Desmet (2022). In contrast to the nearshore CCS, $\sim$1000 km further offshore and in the CNP region, the amplitude of surface $[H^+]$ variability is closer to the magnitude of OA trends (ratio of 1.14 at P_{ONP} and 1.17 at P_{CNP}) leading to the strong and rapid
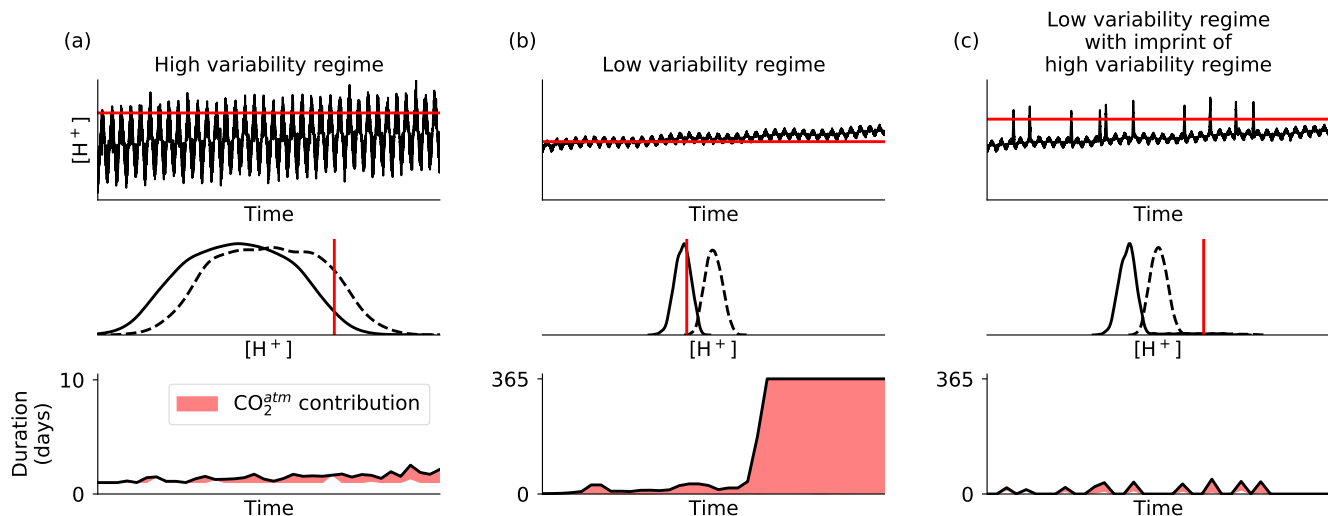
Figure 8. Schematic of three different [H⁺] variability regimes (a-c) that lead to three different responses with regard to OAX under the same long-term increase in [H⁺] from the rise in atmospheric CO_2. (Top) Illustrative 36 years daily time series and their respective 99th percentile threshold computed on the linearly detrended time series. (Middle) Associated probability density functions of the first (solid lines) and last (dashed lines) decades with the same threshold as above (red). (Bottom) Associated annual mean event duration (in days). The red filled area depicts the difference in annual mean event duration between the time series with and without the long-term trend, i.e, illustrating the contribution of atmospheric CO_2 rise to the temporal change in annual mean event duration. Note the different scale in the left plot. A low frequency modulation, representing decadal climate variability, is included in all three signals.

increase in OAX. The more similar amplitudes of variability and trends in these regions is due to a five times smaller surface variability compared to the nearshore CCS (Appendix Fig. B6a-c). Consistent with the even larger and faster increase in yearly OAX days found in the subsurface CNP is the even lower variability over trend ratios in the subsurface CNP (Fig. B6f,i). In the subsurface waters off central CCS (ONP region) however, we found a much weaker increase in OAX. While the amplitude of the variability within the interdecile range is small and comparable to the one of the subsurface CNP, high [H⁺] are episodically reached (Appendix Fig. B6e). These short and episodic high [H⁺] signals have an amplitude above the upper bound of the interdecile range 7.9 (3) times larger than the amplitude of the interdecile range itself at 100 m (200 m) depth, leading to a highly right skewed natural variability distribution (Appendix Fig. B6e). This skewness delays the emergence of OA trend over the threshold (e.g., Fig. 8c), which explains the weaker increase in OAX (Fig. 2h,i and 6e).

In addition to the spatial heterogeneity in the magnitude of OAX increase, the abruptness of the change also varies spatially, with the strongest step increase in OAX occurring in the subsurface CNP (Section 3.5, Fig. 6f). In light of the relative threshold used in this study, such non-linearities imply that marine organisms may suddenly experience much more often conditions at the edge or outside the local environmental conditions to which they tend to be adapted to, with potential deleterious effects on their fitness (Vargas et al., 2017, 2022; Kroeker et al., 2020; Rivest et al., 2017; Cornwall et al., 2020). While the large increase in OAX in low variability regions, such as the subsurface CNP, results from the rapid exceedance of the variability by

OA trends (e.g., Fig. 8b), the non-linearities (step increases) found in those same regions (Section 3.5, Fig. 6f) may result from the concurrent effect of OA trends and synergistic low frequency (decadal to multi-decadal) climate variability, as illustrated in Fig. 8b. Indeed, the occurrence and intensity of OAXs in the CCons simulation correlate with decadal climatic modes such as the North Pacific Gyre Oscillation (Desmet, 2022). Therefore, low frequency climate variability is likely to modulate, i.e., mitigate or amplify in turn, the imprint of OA trends on OAX. In low natural variability regions, the interaction between OA trends and climate variability may be the cause of a sudden wide-spread crossing of the threshold, when both act in the same direction at the time when the mean state approaches the threshold (Fig. 8b). The timing of the step increases in OAXs in our study may therefore relate to the atmospheric forcing, and would probably vary if we were to run a coupled model, which would have its own decadal and year-to-year variability.

Differences in the natural variability of the ocean carbonate chemistry are also reflected in the regionally different ToEs. We find shorter ToE in the surface subtropical oligotrophic gyre (∼16 years), longer ToE in the surface offshore subarctic region (∼25 years), and even longer ToE in surface coastal areas, both along the Alaskan and the U.S. West coast (∼30-32 years to no emergence yet in 2019). The ordering of these results is consistent with results from observations with the station ALOHA in the subtropical oligotrophic gyre having the shortest ToE in the Northeast Pacific (9 years), closely followed by station Papa in the offshore subarctic (10 years), and then by coastal sites (12-23 years) (Sutton et al., 2019). The ToEs found in our study are about 1.5 to 2.5 times larger than those found in Sutton et al. (2019). This is also true when comparing to pCO_2 and pH ToE found in Keller et al. (2014). However, these differences are consistent with the differences in definitions, with our detection threshold being more restrictive than in Keller et al. (2014), and with the absence of seasonal variability in the background monthly variability used by Sutton et al. (2019), as well as the absence of intra-annual variability in Keller et al. (2014).

As pointed out with regard to the emergence of OA trends in Sutton et al. (2019), our study underlines the importance of the natural variability of the ocean carbonate chemistry with respect to the response of OAX to anthropogenic changes. Our results based on a high spatiotemporal resolution model show that the emergence of near permanent OAXs is substantially delayed in coastal regions, as well as quite far offshore at depth in regions that see the mesoscale imprint of nearshore conditions (cf. white areas in Fig. 7).

4.3 Delayed emergence of near permanent subsurface OAX by mesoscale cyclonic eddies

In the subsurface of the ONP region, the shape of OAX (Fig. 1a) and the spatial pattern of annual maximum intensity (Fig. 4d-i) relate to mesoscale eddy tracks (Section 3.3). The distinctive pattern of subsurface maximum intensity does not appear in the analyses of Burger et al. (2020) (cf. Fig. 7d in their manuscript). We also do not expect it to appear, since the resolution of their model is much coarser (horizontal resolution of ∼80 km), preventing it from resolving the mesoscale processes that we identify as shaping this spatial heterogeneities in subsurface OAX maximum intensity. This is consistent with previous findings based on a Lagrangian perspective that found mesoscale cyclonic eddies to be important drivers of OAX in the subsurface of the Northeast Pacific (Desmet et al., 2022). Moreover, the sharp spatial boundaries between short (∼22 years on average) and long (∼32 years on average) ToE in the subsurface, and the corresponding boundaries between large (+248 days on average) and small (+36 days on average) increases in yearly extreme days and annual mean event duration from 1984 to 2019, correspond

well to the westward extent of cyclonic eddy-driven OAXs in the Northeast Pacific (Appendix A, Fig. 6b,c and 7b,c). This result suggests that mesoscale cyclonic eddies substantially enhance the amplitude of the background variability at depth in the open ocean, and, as a result, lead to large threshold values relative to the mean of local $[H^+]$ distributions (Appendix Fig. B6e and A1). This eddy-induced variability substantially delays the ToE of OAX and reduces the increase in yearly extreme days and event duration in comparison to open ocean regions experiencing weak mesoscale activity. This is consistent with our subsurface rates of increase in the number of extreme days and OAX duration being lower than in previous global ocean studies that are based on global Earth system models that do not fully resolve mesoscale variability (Section 4.1).

The cyclonic eddy-driven OAX westward propagation front defined in our study resonates well with previous findings on the offshore imprint of nearshore waters from cyclonic eddies (Zhao et al., 2021; Chabert et al., 2021; Amos et al., 2019; Chenillat et al., 2016; Nagai et al., 2015). They show that cyclonic eddies maintain locally elevated nutrients concentrations, productivity, and organic matter in the offshore more than 1000 km away from the CCS coast. Especially, subsurface coherent eddies originating from the eastern boundary poleward undercurrents ("Puddies") have been shown to contribute to low-oxygen extreme events and to reach thousands of kilometers offshore in the subsurface (Frenger et al., 2018). These Puddies have their core between 100 and 700 m depth, matching the absence of eddy front signal in surface OAX and its presence at 100 and 200 depth. Furthermore, the depth-dependency of our eddy front is consistent with Puddies sliding along isopycnals and subducting from the nearshore formation regions into the gyre interiors (Frenger et al., 2018). Finally, the presence of such eddy front is consistent with mesoscale eddies decaying after a certain distance from the coast (Frenger et al., 2018; Chenillat et al., 2016). However, the exact location of this front may be altered by the non-uniform spatial resolution of the telescopic grid, potentially accelerating the decay of mesoscale eddies in our model as the resolution coarsens.

4.4 Limitations and caveats

As the science of ocean acidity extreme events is only in its early stage, there is no consensus yet on the definition of OAX. In this study we use a common Eulerian event-based framework on a single carbonate variable criterion. Several other definitions have been used in previous works, such as in Desmet et al. (2022) where a Lagrangian approach in three dimensions on a dual variable criterion (pH-Ω_A) was taken to define extremes. We expect the Lagrangian pH-Ω_A extreme events to have similar temporal responses to the increase in atmospheric pCO$_2$ as the ones found in this study. Yet, a few differences might ensue from the dual variable criterion and the Lagrangian framework. The former may lead to a different temporal response of OAX in the surface of the ONP and CNP regions, with an abrupt increase in contrast with the linear increase found in our study. Indeed, in these surface offshore areas, where pH and Ω_A are seasonally out of phase, pH-Ω_A extremes will likely occur only once both variables start to be below the lower bound of their variability in the reference period regardless of the season (Xue et al., 2021; Kwiatkowski and Orr, 2018; Desmet et al., 2022). As regards the Lagrangian framework, since we find near permanent extreme conditions in a large fraction of the upper 250 m of the Northeast Pacific, one can expect a single large Lagrangian OAX to form towards the end of the analysis period, with a mean volume close to the entire volume of the upper 250 m of the Northeast Pacific. This may limit the relevance of the Lagrangian definition of OAX when using fixed baselines

490 on reference periods with past atmospheric pCO$_2$ levels such as preindustrial levels or even levels of a few decades earlier, as in this study, due to the rapid OA trend.

The use of relative thresholds on fixed baselines to define OAX requires the model to accurately capture OA trends since the ratio of the long-term trend to local variability is key in determining the increase in OAX in that case. Giving us confidence in our results are the well captured pH and Ω_A surface trends over the last four decades by our model. Yet, in the subsur-
495 face, simulated dissolved inorganic carbon trends tend to be higher than suggested by observations, even though substantial uncertainties associated with the observation-derived trends exist (Franco et al., 2021). If this model subsurface bias holds up to further scrutiny and for other carbonate variables such as [H$^+$], it would imply a slower increase of subsurface OAX than simulated. Yet our conclusions about the large spatial heterogeneity in the progression of OAX and the abruptness of the onset of the OAX in the far offshore regions would remain unchanged.

500 An alternative to fixed baselines is the use of shifting baseline periods that accounts for changes in the mean state of the marine carbonate system variable of interest over the period for which extremes are analyzed (Burger et al., 2020). In that case, the threshold varies in time, following OA trends. Changes in OAX defined on shifting baselines are therefore not well captured by the ToE concept. What drives their change is rather a modification of the short-term variability, i.e., in the nature of the underlying distribution, of the marine carbonate system variable of interest. This leads to larger disparities in the changes in
505 OAX defined with respect to different carbonate variables than when using fixed baselines (Burger et al., 2020). At the global scale, [H$^+$] extremes defined on shifting baselines exhibit large increases in their volume, duration, and intensity in the upper 200 m depth, whereas Ω_A extremes follow a rather decreasing pathway. In our study, a change from fixed to shifting baseline would result in a slower progression of [H$^+$] extremes over the course of the analysis period. Still, spatially heterogeneous increases in OAX are expected to be found, given the expected different changes in the short-term variability of the carbonate
510 variables between regions and depths, stemming from the many processes in play – e.g., long-term changes in upwelling, eddy activity, buffer factor, or temperature – and their varying relationship with the different carbonate variables. The ecological relevance of using a fixed vs. shifting baseline to define OAX depends on the level of adaptive capacity of marine ecosystems to long-term changes in OA, and on the time scales of this potential adaptation (Oliver, 2019; Oliver et al., 2021; Gruber et al., 2021). Yet the level of adaptive capacity of marine ecosystems to long-term changes in OA is still unclear (Mekkes et al.,
515 2021; Bednaršek et al., 2016, 2017, 2021; Manno et al., 2017). The use of a fixed baseline, as chosen in our study, allows for capturing changes in OAX ensued from both long-term anthropogenic and short-term variability changes, that add up and may together lead to episodic crossings of biological thresholds (Doney et al., 2020; Bednaršek et al., 2017).

In addition to the detection of extremes with regard to [H$^+$], we quantify the proportion of [H$^+$] extremes that are undersaturated with regard to aragonite, since $\Omega_A = 1$ is a well-known threshold for OA impacts on shelled marine organisms such
520 as pteropods (Bednaršek et al., 2014). However, different thresholds may be relevant for different organisms, life stages, and durations of exposure (Bednaršek et al., 2019; Fabry et al., 2008). For instance, supersaturated waters with Ω_A below 1.5 have also been found to cause mild and severe dissolution of pteropods shell (Bednaršek et al., 2019). When quantifying the proportion of OAXs that are in waters with an Ω_A below 1.5, cross-shore and cross-depth patterns similar to those found for a threshold of $\Omega_A = 1$ (section 3.1) were found (Appendix Table B1).

525 As for the undersaturation criterion, most of the surface OAXs and most of the CNP OAXs have Ω_A above 1.5. However, in the CNP 50-100 m depth layers, 1 % of OAX volume have Ω_A levels below 1.5 while none is undersaturated yet (Appendix Table B1 and Table 2). The analysis for $\Omega_A < 1.5$ also reveals that most of the newly undersaturated OAXs found in the 50-100 m depth layer of ACR and CCS occur in waters that were only weakly supersaturated ($\Omega_A < 1.5$) in the CCons simulation (Table 2 and Appendix Table B1). This result is consistent with previous findings on low aragonite saturation state events (i.e.,

530 extremes defined based on absolute thresholds), that show a projected rapid increase in the duration of undersaturation events at the seafloor of the nearshore CCS, already weakly supersaturated with regard to aragonite in the preindustrial period (Ω_A permanently under 1.4; Hauri et al., 2013a). It suggests that organisms hit by newly undersaturated OAXs may already be, in most of the cases, adapted to near-corrosive conditions.

5   Conclusions

535 Our study highlights the rapidity of the increase in ocean acidity extremes, in agreement with previous regional and global scale studies on past and projected changes (Hauri et al., 2013a; Burger et al., 2020; Gruber et al., 2021). What was defined as rare high acidity events in the past, i.e., relative to atmospheric CO_2 concentrations of 1979 in our study, has already become a near permanent state over large areas in the upper 250 m of the Northeast Pacific, although with important regional variations. Knowledge of the impacts of present-day extremes on organisms and ecosystems may therefore offer a glimpse of the future

540 health of the ocean, respectively near future in the surface and the offshore, and more distant future in coastal subsurface regions given the spatial heterogeneity in increasing rates of acidity extremes.

  The increase in ocean acidity extremes from 1984 to 2019 in the Northeast Pacific is mostly driven by the rise of anthropogenic atmospheric CO_2. Present-day trends in ocean acidity extremes will therefore continue as atmospheric CO_2 continues to rise, or even accelerate as the buffer capacity of the seawater declines, especially in regions with already low buffering

545 capacity, such as the Alaskan coast and the nearshore California current system (Cai et al., 2020; Feely et al., 2018; Jiang et al., 2019). This is worrisome in the context of the constantly growing anthropogenic CO_2 emissions (Friedlingstein et al., 2019), especially as a large fraction of these high acidity extremes also cross well-known biological thresholds of aragonite saturation state. Furthermore, non-linearities in the increase of extremes defined on relative thresholds, such as those found in our study, imply that organisms may suddenly experience much more often conditions at the edge or outside the variability

550 range of their local environment. This may lead to deleterious impacts on marine organisms since they tend to be adapted to their local environment and its variability (Vargas et al., 2017; Kroeker et al., 2020; Rivest et al., 2017; Cornwall et al., 2020).

  While the strong ocean acidification trend overtakes the natural variability over large areas in the upper 250 m of the Northeast Pacific, interannual variability still drives the occurrence of acidity extremes in subsurface coastal regions substantially. In the California current system, the El-Niño-Southern-Oscillation is likely to be a strong modulator of ocean acidity extremes

555 on interannaual timescales, since it modulates the biogeochemistry of the region (Turi et al., 2018; Frischknecht et al., 2015). Studies that assess the response of acidity extreme events to climatic modes are needed, and could further be used to forecast the occurrence and intensity of acidity extremes in coastal regions of the Northeast Pacific. Besides interannual variability,

our study uncovers the key role of mesoscale activity in slowing down the increase in acidity extremes in the subsurface of intermediate offshore regions compared to previously found increases in global scale studies (e.g., Burger et al., 2020). This implies that ocean acidity extremes in those regions may increase less rapidly than projected by Earth system models (Burger et al., 2020), since these models often miss the strong variability induced by mesoscale activity.

Data availability. The processed data are available online at the ETH library archive (https://www.research-collection.ethz.ch/handle/20. 500.11850/604737). Model output data may be obtained upon request from the corresponding author (flora.desmet@usys.ethz.ch).

Appendix A: Eddy front definition

We identify the westward eddy propagating front at 100 m and 200 m depth between 28°N and 47°N as the farthest distance to the coast where at least one eddy-driven OAX, i.e., one "Large, Long, and Propagating" (LLP) OAX (Desmet et al., 2022), passes every five years. The rationale for this choice is the following. In offshore regions with small variability range, eddies need to be present more than 1 % of the time to significantly affect the threshold defined as the 99th of all aggregated daily value at a given location, i.e., more than 132 days in our case from 1984 through 2019 (Fig. A1). Eddy-driven OAXs, as found in previous work by Desmet et al. (2022), have an average local duration of 18 days both at 100 m and 200 m depth, meaning that they stay on average 18 days at a given location. Thus, a location must see on average seven of these eddy-driven events over the entire period for its threshold to be substantially moved away from the mean variability range (Fig. A1), i.e., at least one eddy-driven OAX every five years. For each LLP events of Desmet et al. (2022) we first compute its maximum distance to the coast and the associated latitude. We then bin these events based on the latitude at which they are the farthest away from the coast into 1°latitudinal bands between 28°N and 47°N. Within each latitudinal bin we select the seventh maximum distance to the coast to make sure that at least seven eddy-driven OAXs reach this distance from the coast. In a last step we apply a Gaussian smoothing ($\sigma = 2$ °N) to the eddy front.
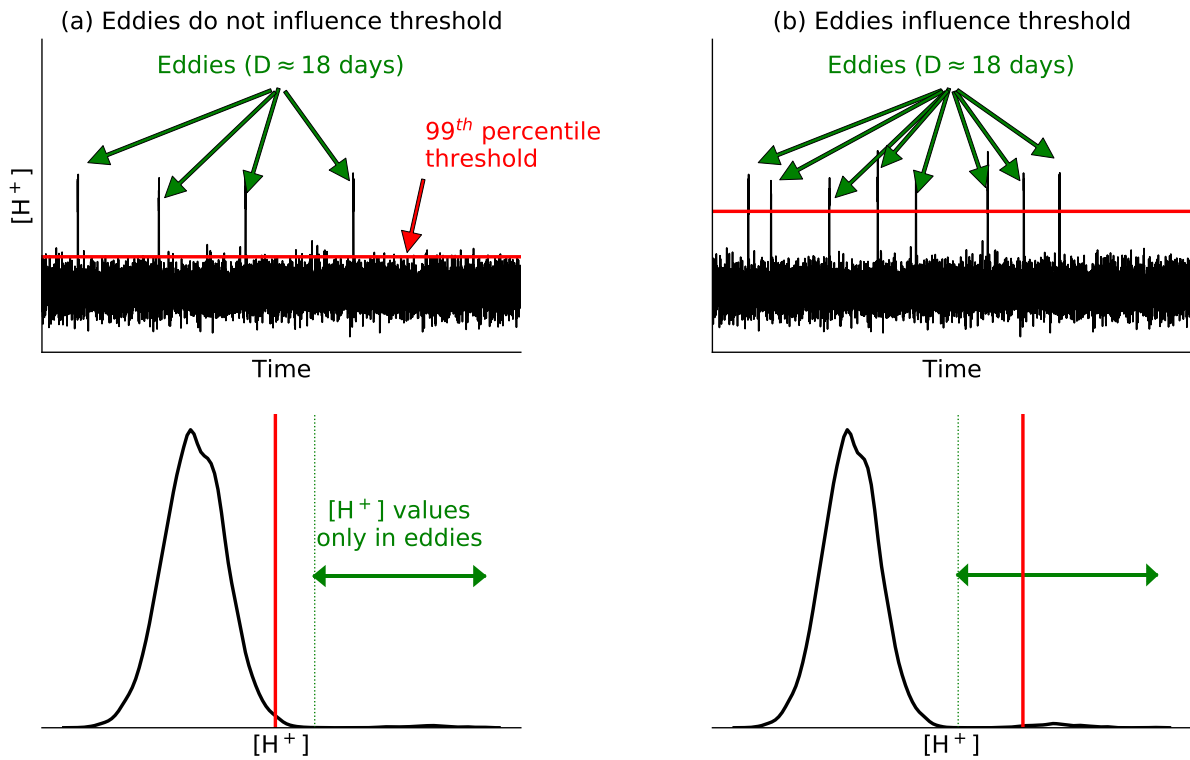
Figure A1. Schematic of [H$^+$] daily variability in (a) a region where the threshold is not influenced by passing mesoscale eddies and (b) a region where the threshold is shifted away from the normal distribution due a high number of passing eddies. In (a), the high [H$^+$] signal carried eddies accounts for less than 1 % of the total days ($\approx$4x18 days $\approx$72 days while 1 % of the days from 1984 to 2019 would be 132 days) and therefore does not influence the threshold that remains below the high [H$^+$] values carried by eddies. In (b), the high [H$^+$] signal of eddies accounts for more than 1 % of the total days ($\approx$8x18 days $\approx$144 days) and therefore raises the threshold to a value within the range of high [H$^+$] values carried by eddies.

Appendix B: Supplementary figures
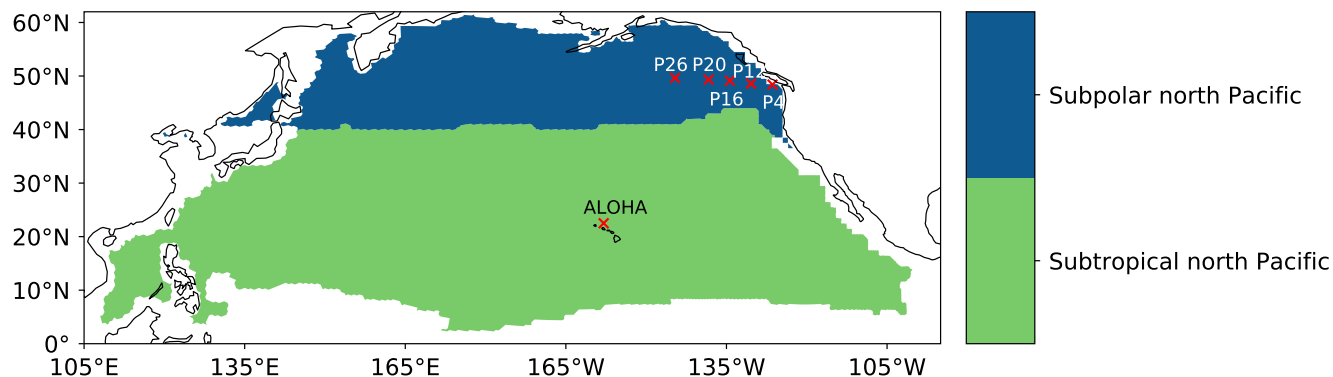
Figure B1. Biomes and stations used to evaluate ROMS-BEC surface pH and Ω_A long-term trends against observations from Lauvset et al. (2015); Franco et al. (2021); Bates et al. (2014) in Table 1.
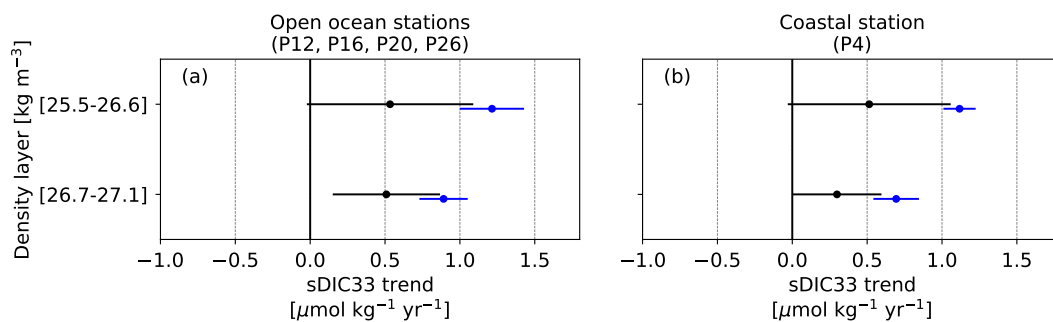
Figure B2. Trends in dissolved inorganic carbon normalized to a salinity value of 33 psu (sDIC33) in the subsurface of line P (in μmol kg^{-1} yr^{-1}). (blue) Simulated ROMS-BEC trends and (black) observed trends from Fig. 6 in Franco et al. (2021). The trends have been averaged within two density layers, namely mixed layer/pycnocline waters ([25.5-26.6] kg m^{-3}) and intermediate waters ([26.7-27.1] kg m^{-3}), as well as across the four open ocean stations (P12, P16, P20, P26) in panel (a). Black error bars denote the average of the two standard deviation credible interval (95 % CrI) of individual data points from Fig. 6 in Franco et al. (2021), while blue error bars denote the spatial standard deviation across stations and density levels from ROMS-BEC simulated trends.
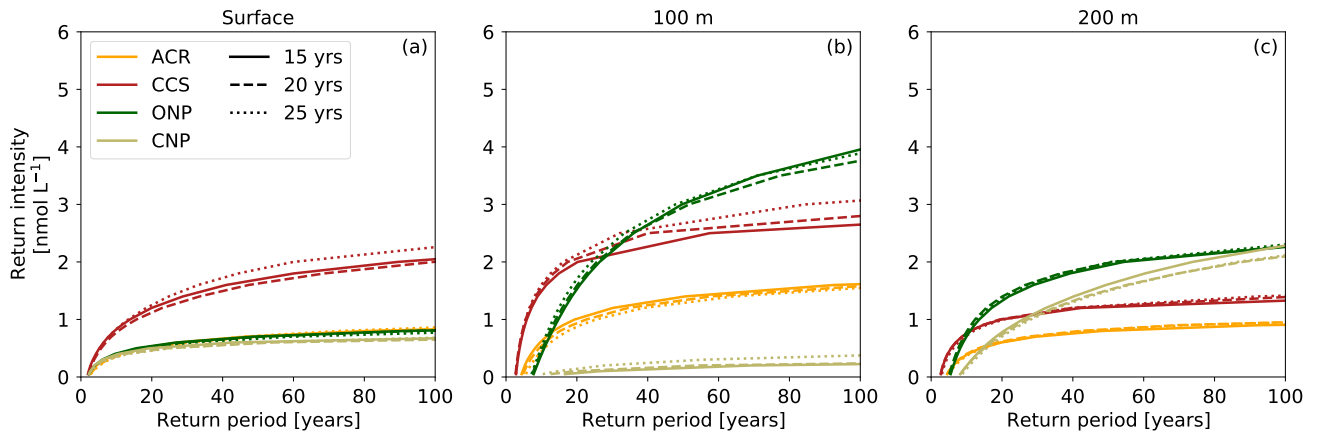
Figure B3. Return intensity (in nmol L^{-1}) as a function of the return period (in years) at the (a) surface, (b) 100 m, and (c) 200 m depth in the ACR, CCS, ONP, and CNP regions and for time periods of length 15 years (solid; 2005-2019), 20 years (dashed; 2000-2019), and 25 years (dotted; 1995-2019) in the CCons simulation. The line represents the median based on the spatial variability within each region.
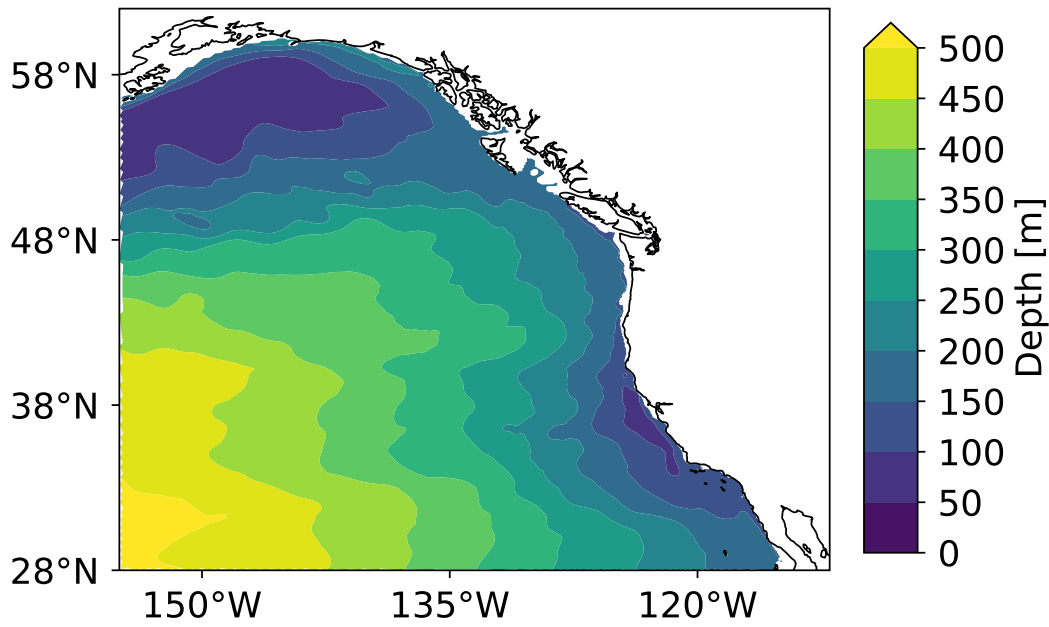
Figure B4. ROMS-BEC simulated climatological (1984-2019) annual mean depths of the Ω_A saturation horizon (Ω_A=1) in the CCons simulation.
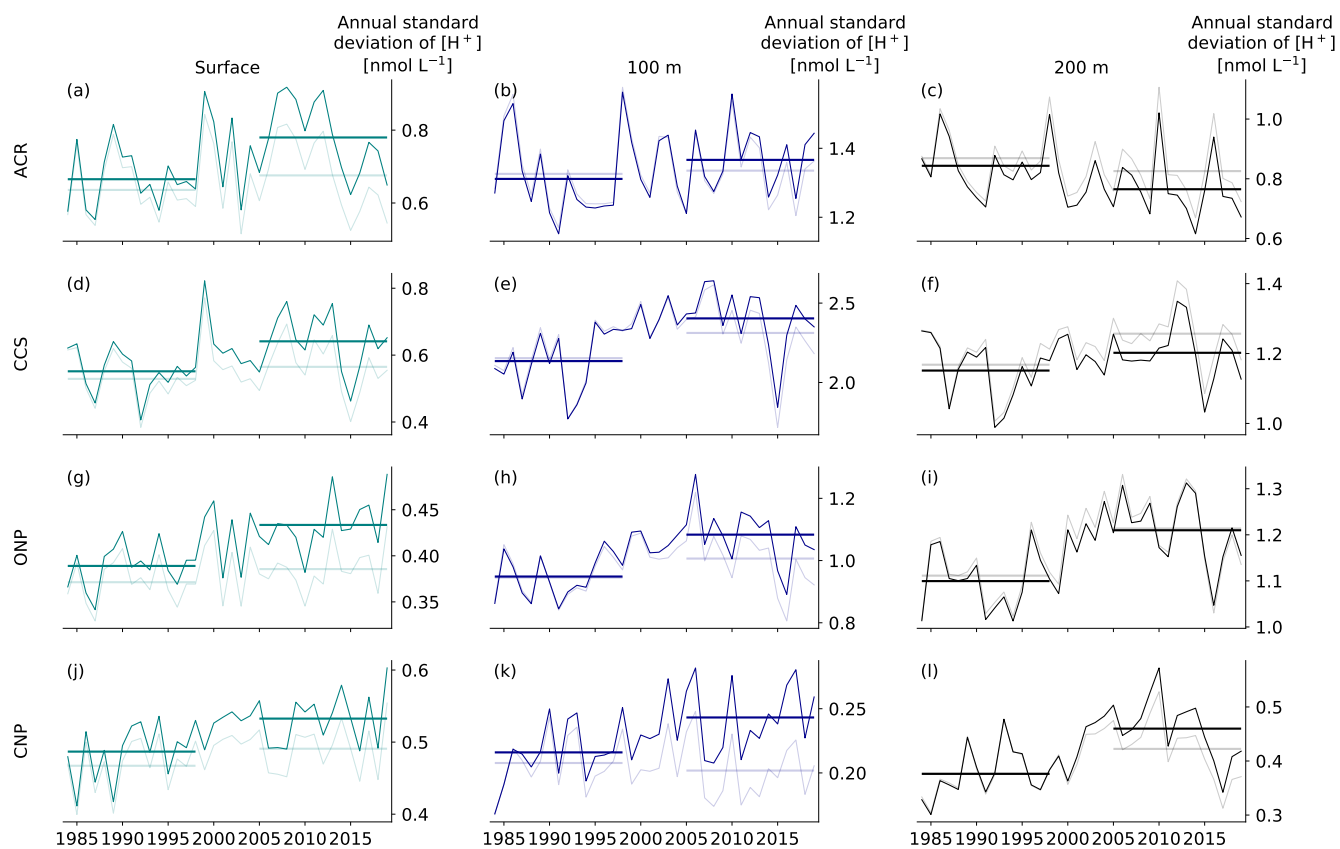
Figure B5. Changes in annual standard deviation of [H$^+$] in the HCast (dark) and CCons (light) simulations for the four regions (rows) and three depth layers (columns). The horizontal lines depict the average standard deviation during the 15 first and last years of the analysis period for each simulation.
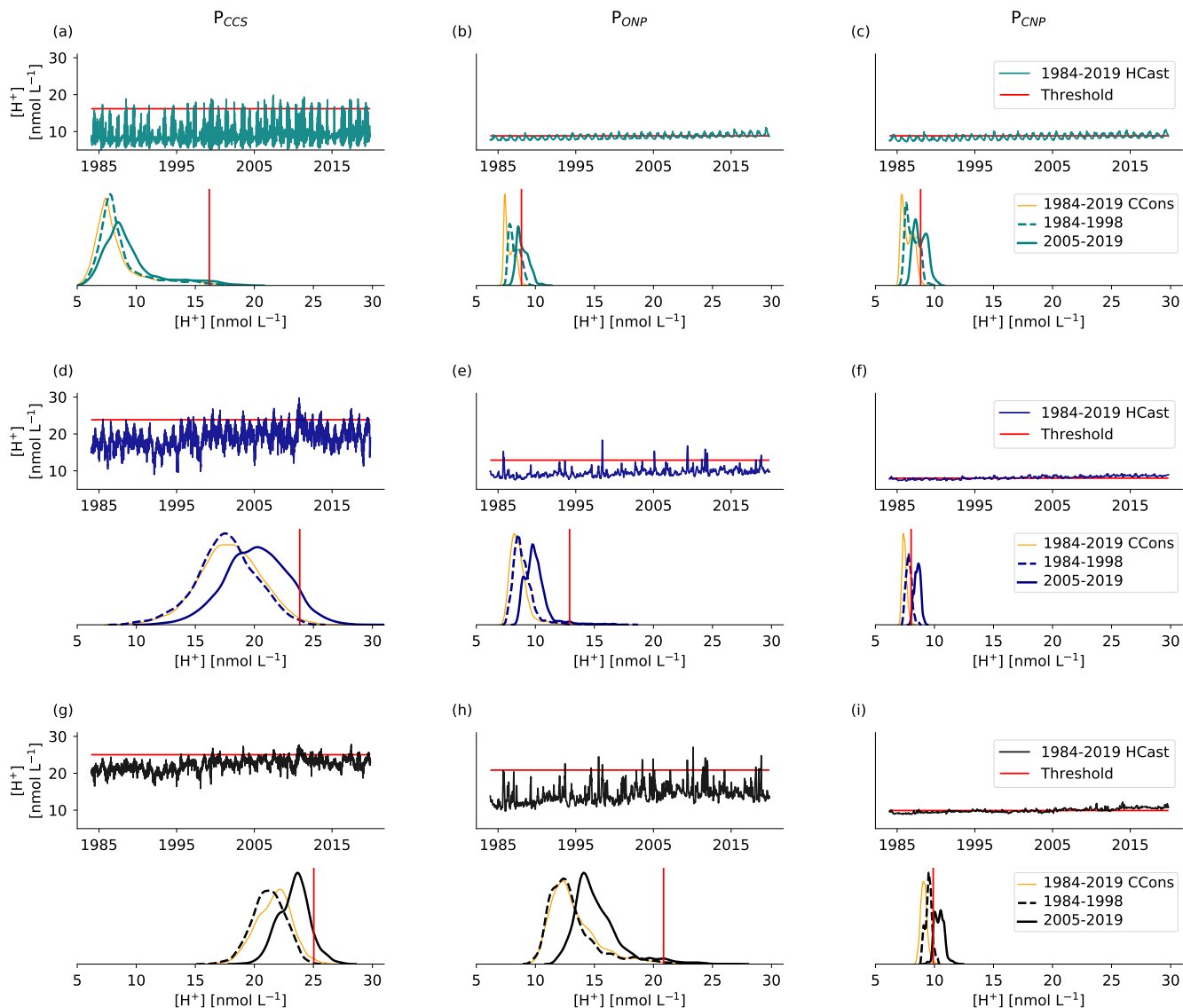
Figure B6. Time series and probability density functions (PDF) of [H$^+$] (nmol L^{-1}) at the three locations plotted in Fig. 6 for (top) surface, (middle) 100 m depth and (bottom) 200 m depth in the HCast simulation. The respective [H$^+$] thresholds are plotted in red. In the PDF plots, the PDF over the entire period (1984-2019) in the CCons simulation is plotted in orange and the PDFs of the 1984-1998 and 2005-2019 periods of the HCast simulation are plotted in cyan, blue, and black depending on the depth with a dashed and solid line respectively. The periods correspond to the periods used for the difference maps in Fig. 4 and 6.

Table B1. Fraction (in %) of the OAX volume that is characterized by $\Omega_A < 1.5$ conditions with regard to aragonite averaged over 1984-2019 for the four different regions of the Northeast Pacific shown in Fig. 1a and for three different depth layers. Numbers in the "Ω_A newly < 1.5" column give the fraction of the OAX volume that is newly in $\Omega_A < 1.5$ conditions with regard to aragonite. This is computed by identifying the fraction of the OAX volume that is in $\Omega_A < 1.5$ conditions in the HCast simulation but in $\Omega_A \geq 1.5$ conditions in the CCons simulation where atmospheric CO_2 was kept at its 1979's value.

	0-50 m		50-100 m		100-250 m	
	Ω_A newly < 1.5	$\Omega_A < 1.5$	Ω_A newly < 1.5	$\Omega_A < 1.5$	Ω_A newly < 1.5	$\Omega_A < 1.5$
Alaskan Coastal Region (ACR)	12	23	1	99	$\ll 1$	100
California Current System (CCS)	<1	7	1	99	0	100
Offshore Northeast Pacific (ONP)	2	2	6	17	8	95
Central Northeast Pacific (CNP)	$\ll 1$	$\ll 1$	1	1	4	10

Author contributions. The conceptualisation of this research was done by all co-authors. FD performed the simulations and conducted the formal analysis. FD prepared the manuscript with contributions from all co-authors.

Competing interests. The authors declare that they have no conflict of interest.

Acknowledgements. This research was supported by the Swiss National Science Foundation under grant agreement No 175787 (Project X-EBUS), by the Swiss Federal Institute of Technology Zürich (ETH Zürich), and by the European Union's Horizon 2020 research and innovation programme under grant agreement No 820989 (project COMFORT). The simulations were performed at the HPC cluster of ETH Zürich, Euler, which is located in the Swiss Supercomputing Center (CSCS) in Lugano and operated by ETH ITS Scientific IT Services in Zürich. All further analyses and all figures were created using the software package Python. We thank Dr. Meike Vogt for her valuable feedback on an earlier version of the manuscript. The authors also thank the two reviewers for their thoughtful and constructive reviews that helped to improve the article.

References

Amos, C. M., Castelao, R. M., and Medeiros, P. M.: Offshore transport of particulate organic carbon in the California Current System by mesoscale eddies, Nature Communications, 10, https://doi.org/https://doi.org/10.1038/s41467-019-12783-5, publisher: Springer US, 2019.

Bates, N. R., Astor, Y. M., Church, M. J., Currie, K., Dore, J. E., González-Dávila, M., Lorenzoni, L., Muller-Karger, F., Olafsson, J., and Santana-Casiano, J. M.: A time-series view of changing surface ocean chemistry due to ocean uptake of anthropogenic CO2 and ocean acidification, Oceanography, 27, 126–141, https://doi.org/https://doi.org/10.5670/oceanog.2014.16, 2014.

Bednaršek, N., Feely, R. A., Reum, J. C. P., Peterson, B., Menkel, J., Alin, S. R., and Hales, B.: Limacina helicina shell dissolution as an indicator of declining habitat suitability owing to ocean acidification in the California Current Ecosystem, Proceedings of the Royal Society B, 281, https://doi.org/https://doi.org/10.1098/rspb.2014.0123, 2014.

Bednaršek, N., Harvey, C. J., Kaplan, I. C., Feely, R. A., and Možina, J.: Pteropods on the edge: Cumulative effects of ocean acidification, warming, and deoxygenation, Progress in Oceanography, 145, 1–24, https://doi.org/https://doi.org/10.1016/J.POCEAN.2016.04.002, publisher: Pergamon, 2016.

Bednaršek, N., Feely, R. A., Tolimieri, N., Hermann, A. J., Siedlecki, S. A., Waldbusser, G. G., Mcelhany, P., Alin, S. R., Klinger, T., Moore-Maley, B., and Pörtner, . H. O.: Exposure history determines pteropod vulnerability to ocean acidification along the US West Coast, Nature Scientific Reports, https://doi.org/https://doi.org/10.1038/s41598-017-03934-z, 2017.

Bednaršek, N., Feely, R. A., Howes, E. L., Hunt, B. P. V., Kessouri, F., León, P., Lischka, S., Maas, A. E., McLaughlin, K., Nezlin, N. P., Sutula, M., and Weisberg, S. B.: Systematic Review and Meta-Analysis Toward Synthesis of Thresholds of Ocean Acidification Impacts on Calcifying Pteropods and Interactions With Warming, Frontiers in Marine Science, 6, https://doi.org/https://doi.org/10.3389/fmars.2019.00227, 2019.

Bednaršek, N., Feely, R. A., Beck, M. W., Alin, S. R., Siedlecki, S. A., Calosi, P., Norton, E. L., Saenger, C., Štrus, J., Greeley, D., Nezlin, N. P., Roethler, M., and Spicer, J. I.: Exoskeleton dissolution with mechanoreceptor damage in larval Dungeness crab related to severity of present-day ocean acidification vertical gradients, Science of the Total Environment, 716, https://doi.org/10.1016/j.scitotenv.2020.136610, 2020.

Bednaršek, N., Naish, K.-A., Feely, R. A., Hauri, C., Kimoto, K., Hermann, A. J., Michel, C., Niemi, A., and Pilcher, D.: Integrated Assessment of Ocean Acidification Risks to Pteropods in the Northern High Latitudes: Regional Comparison of Exposure, Sensitivity and Adaptive Capacity, Frontiers in Marine Science, 8, 1–23, https://doi.org/https://doi.org/10.3389/fmars.2021.671497, 2021.

Bindoff, N. L., Cheung, W. W. L., Kairo, J. G., Arístegui, J., Guinder, V. A., Hallberg, R., Hilmi, N., Jiao, N., Karim, M. S., Levin, L., O'Donoghue, S., Purca Cuicapusa, S. R., Rinkevich, B., Suga, T., Tagliabue, A., and Williamson, P.: Changing Ocean, Marine Ecosystems, and Dependent Communities, in: IPCC Special Report on the Ocean and Cryosphere in a Changing Climate [H.-O. Pörtner, D.C. Roberts, V. Masson-Delmotte, P. Zhai, M. Tignor, E. Poloczanska, K. Mintenbeck, A. Alegría, M. Nicolai, A. Okem, J. Petzold, B. Rama, N.M. Weyer (eds.)]. In press., pp. 447–588, 2019.

Burger, F. A., John, J. G., and Frölicher, T. L.: Increase in ocean acidity variability and extremes under increasing atmospheric CO2, Biogeosciences, pp. 4633–4662, https://doi.org/https://doi.org/10.5194/bg-17-4633-2020, 2020.

Burger, F. A., Terhaar, J., and Frölicher, T. L.: Compound marine heatwaves and ocean acidity extremes, Nature Communications, 13, 4722, https://doi.org/10.1038/s41467-022-32120-7, 2022.

625   Byrne, R. H., Mecking, S., Feely, R. A., and Liu, X.: Direct observations of basin-wide acidification of the North Pacific Ocean, Geophysical Research Letters, https://doi.org/10.1029/2009GL040999, 2010.

Cai, W. J., Xu, Y. Y., Feely, R. A., Wanninkhof, R., Jönsson, B., Alin, S. R., Barbero, L., Cross, J. N., Azetsu-Scott, K., Fassbender, A. J., Carter, B. R., Jiang, L. Q., Pepin, P., Chen, B., Hussain, N., Reimer, J. J., Xue, L., Salisbury, J. E., Hernández-Ayón, J. M., Langdon, C., Li, Q., Sutton, A. J., Chen, C. T. A., and Gledhill, D. K.: Controls on surface water carbonate chemistry along North American ocean

630   margins, Nature Communications, 11, 1–13, https://doi.org/https://doi.org/10.1038/s41467-020-16530-z, 2020.

Caldeira, K. and Wickett, M. E.: Anthropogenic carbon and ocean pH, Nature, 425, 365, https://doi.org/10.1038/425365a, 2003.

Carter, B. R., Williams, N. L., Evans, W., Fassbender, A. J., Barbero, L., Hauri, C., Feely, R. A., and Sutton, A. J.: Time of Detection as a Metric for Prioritizing Between Climate Observation Quality, Frequency, and Duration, Geophysical Research Letters, 46, 3853–3861, https://doi.org/10.1029/2018GL080773, 2019.

635   Chabert, P., d'Ovidio, F., Echevin, V., Stukel, M. R., and Ohman, M. D.: Cross-Shore Flow and Implications for Carbon Export in the California Current Ecosystem: A Lagrangian Analysis, Journal of Geophysical Research: Oceans, 126, 1–14, https://doi.org/10.1029/2020jc016611, 2021.

Chenillat, F., Franks, P. J., and Combes, V.: Biogeochemical properties of eddies in the California Current System, Geophysical Research Letters, 43, 5812–5820, https://doi.org/https://doi.org/10.1002/2016GL068945, 2016.

640   Coles, S.: An Introduction to Statistical Modeling of Extreme Values, Springer-Verlag, London, 2001.

Combes, V., Chenillat, F., Di Lorenzo, E., Rivière, P., Ohman, M., and Bograd, S.: Cross-shore transport variability in the California Current: Ekman upwelling vs. eddy dynamics, Progress in Oceanography, 109, 78–89, https://doi.org/10.1016/j.pocean.2012.10.001, 2013.

Copernicus Climate Change Service (C3S): ERA5: Fifth generation of ECMWF atmospheric reanalyses of the global climate, Copernicus Climate Change Service Climate Data Store (CDS),29/08/2020, 2017.

645   Cornwall, C. E., Comeau, S., DeCarlo, T. M., Larcombe, E., Moore, B., Giltrow, K., Puerzer, F., D'Alexis, Q., and McCulloch, M. T.: A coralline alga gains tolerance to ocean acidification over multiple generations of exposure, Nature Climate Change, 10, 143–146, https://doi.org/https://doi.org/10.1038/s41558-019-0681-8, 2020.

Desmet, F.: Ocean acidity extremes and their spatiotemporal evolution, a high-resolution modeling study in the northeast Pacific, Ph.D. thesis, ETH Zürich, https://doi.org/10.3929/ethz-b-000598701, 2022.

650   Desmet, F., Gruber, N., Köhn, E. E., Münnich, M., and Vogt, M.: Tracking the space-time evolution of ocean acidification extremes in the California Current System and Northeast Pacific, Journal of Geophysical Research: Oceans, pp. 1–30, https://doi.org/10.1029/2021jc018159, 2022.

Doney, S. C., Fabry, V. J., Feely, R. A., and Kleypas, J. A.: Ocean Acidification: The Other CO2 Problem, Annual Review of Marine Science, 1, 169–192, https://doi.org/https://doi.org/10.1146/annurev.marine.010908.163834, 2009.

655   Doney, S. C., Busch, D. S., Cooley, S. R., and Kroeker, K. J.: The Impacts of Ocean Acidification on Marine Ecosystems and Reliant Human Communities, Annual Review of Environment and Resources, pp. 1–30, https://doi.org/https://doi.org/10.1146/annurev-environ-012320-083019, 2020.

Fabry, V. J., Seibel, B. A., Feely, R. A., and Orr, J. C.: Impacts of ocean acidification on marine fauna and ecosystem processes, in: ICES Journal of Marine Science, vol. 65, pp. 414–432, https://doi.org/https://doi.org/10.1093/icesjms/fsn048, 2008.

660   Fassbender, A. J., Sabine, C. L., Feely, R. A., Langdon, C., and Mordy, C. W.: Inorganic carbon dynamics during northern California coastal upwelling, Continental Shelf Research, https://doi.org/https://doi.org/10.1016/j.csr.2011.04.006, 2011.

Fassbender, A. J., Alin, S. R., Feely, R. A., Sutton, A. J., Newton, J. A., Krembs, C., Bos, J., Keyzers, M., Devol, A., Ruef, W., and Pelletier, G.: Seasonal carbonate chemistry variability in marine surface waters of the US Pacific Northwest, Earth Syst. Sci. Data, 10, 1367–1401, https://doi.org/https://doi.org/10.5194/essd-10-1367-2018, 2018.

665 Feely, R. A. and Chen, A.: The effect of excess CO2 on the calculated calcite and aragonite saturation horizons in the northeast Pacific, 9, 1294–1297, 1982.

Feely, R. A., Sabine, C. L., Hernandez-Ayon, J. M., Ianson, D., and Hales, B.: Evidence for upwelling of corrosive "acidified" water onto the continental shelf., Science, 320, 1490–2, https://doi.org/https://doi.org/10.1126/science.1155676, 2008.

Feely, R. A., Okazaki, R. R., Cai, W.-J., Bednaršek, N., Alin, S. R., Byrne, R. H., and Fassbender, A.: The combined effects of acidification
670 and hypoxia on pH and aragonite saturation in the coastal waters of the California current ecosystem and the northern Gulf of Mexico, Continental Shelf Research, 152, 50–60, https://doi.org/10.1016/j.csr.2017.11.002, 2018.

Franco, A. C., Gruber, N., Frölicher, T. L., and Kropuenske Artman, L.: Contrasting Impact of Future CO2 Emission Scenarios on the Extent of CaCO3 Mineral Undersaturation in the Humboldt Current System, Journal of Geophysical Research: Oceans, pp. 2018–2036, https://doi.org/https://doi.org/10.1002/2018JC013857, iSBN: 21699275, 2018.

675 Franco, A. C., Ianson, D., Ross, T., Hamme, R. C., Monahan, A. H., Christian, J. R., Davelaar, M., Johnson, W. K., Miller, L. A., Robert, M., and Tortell, P. D.: Anthropogenic and Climatic Contributions to Observed Carbon System Trends in the Northeast Pacific, Global Biogeochemical Cycles, 35, 1–21, https://doi.org/10.1029/2020GB006829, 2021.

Frenger, I., Bianchi, D., Stührenberg, C., Oschlies, A., Dunne, J., Deutsch, C., Galbraith, E., and Schütte, F.: Biogeochemical role of sub-surface coherent eddies in the ocean: Tracer cannonballs, hypoxic storms, and microbial stewpots?, Global Biogeochemical Cycles, pp.
680 226–249, https://doi.org/https://doi.org/10.1002/2017GB005743, 2018.

Friedlingstein, P., Jones, M. W., O'Sullivan, M., Andrew, R. M., Hauck, J., Peters, G. P., Peters, W., Pongratz, J., Sitch, S., Le Quéré, C., Bakker, D. C. E., Canadell, J. G., Ciais, P., Jackson, R. B., Anthoni, P., Barbero, L., Bastos, A., Bastrikov, V., Becker, M., Bopp, L., Buitenhuis, E., Chandra, N., Chevallier, F., Chini, L. P., Currie, K. I., Feely, R. A., Gehlen, M., Gilfillan, D., Gkritzalis, T., Goll, D. S., Gruber, N., Gutekunst, S., Harris, I., Haverd, V., Houghton, R. A., Hurtt, G., Ilyina, T., Jain, A. K., Joetzjer, E., Kaplan, J. O., Kato, E.,
685 Klein Goldewijk, K., Korsbakken, J. I., Landschützer, P., Lauvset, S. K., Lefèvre, N., Lenton, A., Lienert, S., Lombardozzi, D., Marland, G., McGuire, P. C., Melton, J. R., Metzl, N., Munro, D. R., Nabel, J. E. M. S., Nakaoka, S.-I., Neill, C., Omar, A. M., Ono, T., Peregon, A., Pierrot, D., Poulter, B., Rehder, G., Resplandy, L., Robertson, E., Rödenbeck, C., Séférian, R., Schwinger, J., Smith, N., Tans, P. P., Tian, H., Tilbrook, B., Tubiello, F. N., van der Werf, G. R., Wiltshire, A. J., and Zaehle, S.: Global Carbon Budget 2019, Earth System Science Data, 11, 1783–1838, https://doi.org/10.5194/essd-11-1783-2019, 2019.

690 Frischknecht, M., Münnich, M., and Gruber, N.: Remote versus local influence of ENSO on the California Current System, Journal of Geophysical Research: Oceans, https://doi.org/10.1002/2014JC010531, 2015.

Frischknecht, M., Münnich, M., and Gruber, N.: Origin, Transformation, and Fate: The Three-Dimensional Biological Pump in the California Current System, Journal of Geophysical Research: Oceans, https://doi.org/https://doi.org/10.1029/2018JC013934, 2018.

Gruber, N., Hauri, C., Lachkar, Z., Loher, D., Frolicher, T. L., and Plattner, G.-K.: Rapid Progression of Ocean Acidification in the California
695 Current System, Science, 337, 220–223, https://doi.org/https://doi.org/10.1126/science.1216773, 2012.

Gruber, N., Boyd, P. W., Frölicher, T. L., and Vogt, M.: Biogeochemical extremes and compound events in the ocean, Nature, 600, 395–407, https://doi.org/https://doi.org/10.1038/s41586-021-03981-7, 2021.

Hauri, C., Gruber, N., McDonnell, A. M. P., and Vogt, M.: The intensity, duration, and severity of low aragonite saturation state events on the California continental shelf, Geophysical Research Letters, 40, 3424–3428, https://doi.org/https://doi.org/10.1002/grl.50618, 2013a.

700 Hauri, C., Gruber, N., Vogt, M., Doney, S. C., Feely, R. A., Lachkar, Z., Leinweber, A., McDonnell, A. M., and Munnich, M.: Spatiotemporal variability and long-term trends of ocean acidification in the California Current System, Biogeosciences, 10, 193–216, https://doi.org/https://doi.org/10.5194/bg-10-193-2013, 2013b.

Hauri, C., Friedrich, T., and Timmermann, A.: Abrupt onset and prolongation of aragonite undersaturation events in the Southern Ocean, Nature Climate Change, 6, 172–176, https://doi.org/https://doi.org/10.1038/nclimate2844, 2015.

705 Hersbach, H., Bell, B., Berrisford, P., Hirahara, S., Horányi, A., Muñoz-Sabater, J., Nicolas, J., Peubey, C., Radu, R., Schepers, D., Simmons, A., Soci, C., Abdalla, S., Abellan, X., Balsamo, G., Bechtold, P., Biavati, G., Bidlot, J., Bonavita, M., De Chiara, G., Dahlgren, P., Dee, D., Diamantakis, M., Dragani, R., Flemming, J., Forbes, R., Fuentes, M., Geer, A., Haimberger, L., Healy, S., Hogan, R. J., Hólm, E., Janisková, M., Keeley, S., Laloyaux, P., Lopez, P., Lupu, C., Radnoti, G., de Rosnay, P., Rozum, I., Vamborg, F., Villaume, S., and Thépaut, J. N.: The ERA5 global reanalysis, Quarterly Journal of the Royal Meteorological Society, 146, 1999–2049,
710 https://doi.org/https://doi.org/10.1002/qj.3803, 2020.

Hoegh-Guldberg, O., Jacob, D., Taylor, M., Bindi, M., Brown, S., Camilloni, I., Diedhiou, A., Djalante, R., Ebi, K., Engelbrecht, F., Guiot, J., Hijioka, Y., Mehrotra, S., Payne, A., Seneviratne, S., Thomas, A., Warren, R., and Zhou, G.: Impacts of 1.5°C Global Warming on Natural and Human Systems, in: Global Warming of 1.5°C. An IPCC Special Report on the impacts of global warming of 1.5°C above pre-industrial levels and related global greenhouse gas emission pathways, in the context of strengthening the global response to the threat
715 of climate change, sustainable development, and efforts to eradicate poverty [Masson-Delmotte,V., P. Zhai, H.-O. Pörtner, D. Roberts, J. Skea, P.R. Shukla,A. Pirani,W. Moufouma-Okia, C. Péan, R. Pidcock, S. Connors, J.B.R. Matthews, Y. Chen, X. Zhou, M.I. Gomis, E. Lonnoy, T. Maycock, M. Tignor, and T. Waterfield (eds.)], pp. 175–312, Cambridge University Press, Cambridge, UK and New York, NY, USA, https://doi.org/10.1017/9781009157940.005, 2018.

Jiang, L. Q., Feely, R. A., Carter, B. R., Greeley, D. J., Gledhill, D. K., and Arzayus, K. M.: Climatological distribution of aragonite saturation
720 state in the global oceans, Global Biogeochemical Cycles, https://doi.org/10.1002/2015GB005198, 2015.

Jiang, L. Q., Carter, B. R., Feely, R. A., Lauvset, S. K., and Olsen, A.: Surface ocean pH and buffer capacity: past, present and future, Scientific Reports, 9, 1–11, https://doi.org/https://doi.org/10.1038/s41598-019-55039-4, 2019.

Keller, K. M., Joos, F., and Raible, C. C.: Time of emergence of trends in ocean biogeochemistry, Biogeosciences, 11, 3647–3659, https://doi.org/10.5194/bg-11-3647-2014, 2014.

725 Kroeker, K. J., Bell, L. E., Donham, E. M., Hoshijima, U., Lummis, S., Toy, J. A., and Willis-Norton, E.: Ecological change in dynamic environments: Accounting for temporal environmental variability in studies of ocean change biology, Global Change Biology, pp. 26:54–67, https://doi.org/https://doi.org/10.1111/gcb.14868, 2020.

Kwiatkowski, L. and Orr, J. C.: Diverging seasonal extremes for ocean acidification during the twenty-first century, Nature Climate Change, 8, 141–145, https://doi.org/https://doi.org/10.1038/s41558-017-0054-0, 2018.

730 Landschützer, P., Laruelle, G. G., Roobaert, A., and Regnier, P.: A uniform pCO2 climatology combining open and coastal oceans, Earth System Science Data, 12, 2537–2553, https://doi.org/https://doi.org/10.5194/essd-12-2537-2020, 2020.

Laufkötter, C., Zscheischler, J., and Frölicher, T. L.: High-impact marine heatwaves attributable to human-induced global warming, Science, 369, 1621–1625, https://doi.org/10.1126/science.aba0690, 2020.

Lauvset, S. K., Gruber, N., Landschützer, P., Olsen, A., and Tjiputra, J.: Trends and drivers in global surface ocean pH over the past 3 decades,
735 Biogeosciences, 12, 1285–1298, https://doi.org/https://doi.org/10.5194/bg-12-1285-2015, 2015.

Long, W. C., Swiney, K. M., and Foy, R. J.: Effects of high pCO2 on Tanner crab reproduction and early life history, Part II: carryover effects on larvae from oogenesis and embryogenesis are stronger than direct effects, ICES Journal of Marine Science, 73, 836–848, https://doi.org/10.1093/icesjms/fsv251, 2016.

Ma, D., Gregor, L., and Gruber, N.: Observation-based trends and drivers of global surface ocean acidification over the past four decades, https://doi.org/DOI: 10.22541/essoar.167870335.58952668/v1, 2023.

Manno, C., Bednaršek, N., Tarling, G. A., Peck, V. L., Comeau, S., Adhikari, D., Bakker, D. C., Bauerfeind, E., Bergan, A. J., Berning, M. I., Buitenhuis, E., Burridge, A. K., Chierici, M., Flöter, S., Fransson, A., Gardner, J., Howes, E. L., Keul, N., Kimoto, K., Kohnert, P., Lawson, G. L., Lischka, S., Maas, A., Mekkes, L., Oakes, R. L., Pebody, C., Peijnenburg, K. T., Seifert, M., Skinner, J., Thibodeau, P. S., Wall-Palmer, D., and Ziveri, P.: Shelled pteropods in peril: Assessing vulnerability in a high CO2 ocean, Earth-Science Reviews, 169, 132–145, https://doi.org/https://doi.org/10.1016/j.earscirev.2017.04.005, 2017.

Mekkes, L., Renema, W., Bednaršek, N., Alin, S. R., Feely, R. A., Huisman, J., Roessingh, P., and Peijnenburg, K. T. C. A.: Pteropods make thinner shells in the upwelling region of the California Current Ecosystem, Scientific Reports, 11, 1–11, https://doi.org/https://doi.org/10.1038/s41598-021-81131-9, 2021.

Messié, M., Ledesma, J., Kolber, D. D., Michisaki, R. P., Foley, D. G., and Chavez, F. P.: Potential new production estimates in four eastern boundary upwelling ecosystems, Progress in Oceanography, 83, 151–158, https://doi.org/https://doi.org/10.1016/j.pocean.2009.07.018, 2009.

Moore, J. K., Lindsay, K., Doney, S. C., Long, M. C., and Misumi, K.: Marine Ecosystem Dynamics and Biogeochemical Cycling in the Community Earth System Model [CESM1(BGC)]: Comparison of the 1990s with the 2090s under the RCP4.5 and RCP8.5 scenarios, Journal of Climate, 26, 9291–9312, https://doi.org/https://doi.org/10.1175/JCLI-D-12-00566.1, arXiv: cs/9605103 ISBN: 0894-8755, 2013.

Mundy, P.: The Gulf of Alaska: biology and oceanography, university of Alaska, Alaska Sea Grant College Program, Fairbanks, AK, 2005.

Nagai, T., Gruber, N., Frenzel, H., Lachkar, Z., McWilliams, J. C., and Plattner, G. K.: Dominant role of eddies and filaments in the offshore transport of carbon and nutrients in the California Current System, Journal of Geophysical Research: Oceans, https://doi.org/https://doi.org/10.1002/2015JC010889, 2015.

Negrete-García, G., Lovenduski, N. S., Hauri, C., Krumhardt, K. M., and Lauvset, S. K.: Sudden emergence of a shallow aragonite saturation horizon in the Southern Ocean, Nature Climate Change, 9, 313–317, https://doi.org/10.1038/s41558-019-0418-8, 2019.

Oliver, E. C.: Mean warming not variability drives marine heatwave trends, Climate Dynamics, 53, 1653–1659, https://doi.org/10.1007/s00382-019-04707-2, publisher: Springer Berlin Heidelberg ISBN: 0123456789, 2019.

Oliver, E. C., Benthuysen, J. A., Darmaraki, S., Donat, M. G., Hobday, A. J., Holbrook, N. J., Schlegel, R. W., and Sen Gupta, A.: Marine Heatwaves, Annual Review of Marine Science, 13, 313–342, https://doi.org/https://doi.org/10.1146/annurev-marine-032720-095144, 2021.

Pauly, D. and Christensen, V.: Primary production required to sustain global fisheries, Nature, 374, 255–257, 1995.

Rivest, E. B., Comeau, S., and Cornwall, C. E.: The Role of Natural Variability in Shaping the Response of Coral Reef Organisms to Climate Change, Current Climate Change Reports, 3, 271–281, https://doi.org/https://doi.org/10.1007/s40641-017-0082-x, 2017.

Seneviratne, S. I., Nicholls, N., Easterling, D., Goodness, C. M., Kanae, S., Kossin, J., Luo, Y., Marengo, J., McInnes, K., Rahimi, M., Reichstein, M., Sorteberg, A., Vera, C., and Zhang, X.: Changes in climate extremes and their impacts on the natural physical environment., in: Managing the Risks of Extreme Events and Disasters to Advance Climate Change Adaptation [Field, C.B., V. Barros, T.F. Stocker, D. Qin, D.J. Dokken, K.L. Ebi, M.D. Mastrandrea, K.J. Mach, G.-K. Plattner, S.K. Allen, M. Tignor, and P.M. Midgley (eds.)]. A Special

Report of Working Groups I and II of the Intergovernmental Panel on Climate Change (IPCC), pp. 109–230, Cambridge University Press, Cambridge, UK, and New York, NY, USA, 2012.

775 Shchepetkin, A. F. and McWilliams, J. C.: The regional oceanic modeling system (ROMS): A split-explicit, free-surface, topography-following-coordinate oceanic model, Ocean Modelling, 9, 347–404, https://doi.org/https://doi.org/10.1016/j.ocemod.2004.08.002, iSBN: 1463-5003, 2005.

Sutton, A. J., Feely, R. A., Maenner-Jones, S., Musielwicz, S., Osborne, J., Dietrich, C., Monacci, N., Cross, J., Bott, R., Kozyr, A., Andersson, A. J., Bates, N. R., Cai, W. J., Cronin, M. F., De Carlo, E. H., Hales, B., Howden, S. D., Lee, C. M., Manzello, D. P., McPhaden,
780 M. J., Meléndez, M., Mickett, J. B., Newton, J. A., Noakes, S. E., Noh, J. H., Olafsdottir, S. R., Salisbury, J. E., Send, U., Trull, T. W., Vandemark, D. C., and Weller, R. A.: Autonomous seawater pCO2 and pH time series from 40 surface buoys and the emergence of anthropogenic trends, Earth System Science Data, 11, 421–439, https://doi.org/https://doi.org/10.5194/essd-11-421-2019, 2019.

Swiney, K. M., Long, W. C., and Foy, R. J.: Effects of high pCO2 on Tanner crab reproduction and early life history—Part I: long-term exposure reduces hatching success and female calcification, and alters embryonic development, ICES Journal of Marine Science, 73,
785 825–835, https://doi.org/10.1093/icesjms/fsv201, 2016.

Turi, G., Lachkar, Z., and Gruber, N.: Spatiotemporal variability and drivers of pCO2 and air-sea CO2 fluxes in the California Current System: An eddy-resolving modeling study, Biogeosciences, 11, 671–690, https://doi.org/https://doi.org/10.5194/bg-11-671-2014, 2014.

Turi, G., Lachkar, Z., Gruber, N., and Münnich, M.: Climatic modulation of recent trends in ocean acidification in the California Current System, Environmental Research Letters, 11, 1–17, https://doi.org/https://doi.org/10.1088/1748-9326/11/1/014007, 2016.

790 Turi, G., Alexander, M., Lovenduski, N. S., Capotondi, A., Scott, J., Stock, C., Dunne, J., John, J., and Jacox, M.: Response of O2 and pH to ENSO in the California Current System in a high-resolution global climate model, Ocean Science, 14, 69–86, https://doi.org/10.5194/os-14-69-2018, 2018.

Turk, D., Wang, H., Hu, X., Gledhill, D. K., Wang, Z. A., Jiang, L., and Cai, W.-J.: Time of Emergence of Surface Ocean Carbon Dioxide Trends in the North American Coastal Margins in Support of Ocean Acidification Observing System Design, Frontiers in Marine Science,
795 6, https://doi.org/10.3389/fmars.2019.00091, 2019.

Vargas, C. A., Lagos, N. A., Lardies, M. A., Duarte, C., Manríquez, P. H., Aguilera, V. M., Broitman, B., Widdicombe, S., and Dupont, S.: Species-specific responses to ocean acidification should account for local adaptation and adaptive plasticity, Nature Ecology and Evolution, 1, 1–7, https://doi.org/https://doi.org/10.1038/s41559-017-0084, 2017.

Vargas, C. A., Cuevas, L. A., Broitman, B. R., San Martin, V. A., Lagos, N. A., Gaitán-Espitia, J. D., and Dupont, S.: Upper environmental
800 pCO2 drives sensitivity to ocean acidification in marine invertebrates, Nature Climate Change, 12, https://doi.org/10.1038/s41558-021-01269-2, 2022.

Williams, C. R., Dittman, A. H., McElhany, P., Busch, D. S., Maher, M. T., Bammler, T. K., MacDonald, J. W., and Gallagher, E. P.: Elevated CO 2 impairs olfactory-mediated neural and behavioral responses and gene expression in ocean-phase coho salmon (Oncorhynchus kisutch), Global Change Biology, 25, 963–977, https://doi.org/10.1111/gcb.14532, 2019.

805 Xue, L., Cai, W., Jiang, L., and Wei, Q.: Why are surface ocean pH and CaCO 3 saturation state often out of phase in spatial patterns and seasonal cycles?, Global Biogeochemical Cycles, pp. 1–16, https://doi.org/https://doi.org/10.1029/2021gb006949, 2021.

Zhao, D., Xu, Y., Zhang, X., and Huang, C.: Global chlorophyll distribution induced by mesoscale eddies, Remote Sensing of Environment, 254, 112 245, https://doi.org/10.1016/j.rse.2020.112245, 2021.